Energy 226 (2021) 120441

Contents lists available at ScienceDirect

Energy

journal homepage: www.elsevier.com/locate/energy

Direct-fired oxy-combustion supercritical-CO_2 power cycle with novel preheating configurations -thermodynamic and exergoeconomic analyses

Ahmad K. Sleiti [a, *], Wahib Al-Ammari [a], Samer Ahmed [a], Jayanta Kapat [b]

[a] Department of Mechanical & Industrial Engineering, College of Engineering, Qatar University, Doha, Qatar
[b] Department of Mechanical and Aerospace Engineering, Director of CATER, University of Central Florida, Orlando, USA

ARTICLE INFO

Article history:
Received 1 October 2020
Received in revised form
28 January 2021
Accepted 17 March 2021
Available online 22 March 2021

Keywords:
Supercritical
Carbon dioxide
Preheater
sCO2 power cycle
Oxy-combustion
Dry-cooling

ABSTRACT

Energy, exergy, and exergoeconomic analyses of novel direct-fired oxy-fuel combustion supercritical CO_2 cycle with preheating and dry-cooling are introduced. Novelty aspects of the study include the preheating process effect on the performance of sCO_2 cycle fired by oxy-combustor at moderate turbine inlet temperatures. Three cycles are investigated; original layout without-preheater (configuration M1), integrated preheater with the system in parallel with low-temperature recuperator (configuration M2) and integrated preheater in parallel with both high and low-temperature recuperators (configuration M3). Results show that the integrated preheating process improves cycle efficiency by 3.7% in M2 and by 8.3% in M3. The preheating improves the performance of recuperator by reducing the "pinch-point" effect as a result of the split flow downstream the compressor. The optimization of the split ratio resulted in cycle efficiency of 45.8% in M3, 41.2% in M2, and 37.5% in M1 for $50MW_e$ system at 750 °C turbine inlet temperature. The overall exergy efficiency is improved from 78.1% in M1 to 86.5% in M2 and 88.8% in M3. The exergoeconomic analysis; the first applied to direct-fired oxy-fuel sCO_2 cycle, showed reduction in total product cost per unit exergy by 13.92% in M2 and 34.96% in M3.

1. Introduction

Supercritical carbon dioxide (sCO_2) power cycle is a promising technology for addressing worldwide energy production efficiency and environmental concerns [1] in parallel with other renewables [2–5]. The technology is capable of capturing CO_2 automatically when it is directly fired using natural gas and produces little or no emissions when combined indirectly with renewables [6]. Moreover, sCO_2 cycle has high power efficiency compared to conventional Brayton and Rankine power cycles [7] within the range of medium turbine inlet temperature (500 °C–700 °C) [8]. Besides, it combines the advantages of conventional steam and gas power plants [9] and operates at high pressures with more compact components. Furthermore, the utilization of sCO_2 as a working fluid provides stability and safety for power systems in addition to versatile applications [10].

In the 1940s, the CO_2 power cycle was proposed as a transcritical cycle by Sulzer [11]. About twenty years later, Angelino [12] and Feher [13] presented the fundamentals of the sCO_2 power cycle. Angelino [12] proposed various layouts of transcritical CO_2 cycles, while [13] proposed purely sCO_2 cycles. However, this technology was almost abandoned until 2004 when Dostal [14] proposed it for new generation of nuclear reactors. Several studies have investigated hybrid sCO_2 power systems with various renewable energies such as solar [15–19], geothermal [20,21], and nuclear. Also, it can be powered by waste heat as an integrated cycle with moderate to high-temperature waste heat [22–25] at moderate turbine inlet temperature (TIT) within the range 500 °C to 600 °C [8].

Fossil fuels are the major resource of worldwide energy [26] and their combustion products result in environmental pollution and greenhouse effects. So, development of sCO_2 technology suggests a solution by introducing direct semi-closed oxy-combustion cycles such as Allam cycle [27]. The cycle is developed by 8 Rivers Capital and combines oxy-combustion with sCO_2 cycle. Its major advantages are its ability to capture the produced CO_2 from the oxy-combustion process and its high power cycle efficiency. To investigate its feasibility and to prove the design and operation of the whole cycle, a $50MW_{th}$ natural gas demonstration plant is built in

* Corresponding author.
E-mail address: asleiti@qu.edu.qa (A.K. Sleiti).

https://doi.org/10.1016/j.energy.2021.120441
0360-5442/

Nomenclature

Symbol	Description	Units
A_{HTR}, A_{LTR}	Heat transfer area of high/low-temperature recuperator (HTR/LTR).	m^2
A_{pc}, A_{ph}	Area of precooler, preheater	m^2
$\dot{C}_{D,k}$	Cost rate of exergy destruction-component k	$/h
$\dot{C}_{in,k}$ $\dot{C}_{out,k}$	Cost rate of stream(s) entering, exiting component k	$/h
$\dot{C}_{po,k}$/ $\dot{C}_{q,k}$	Cost rate associated with power output from/heat input into component k	$/h
$cp_{avg,h,i}$/$cp_{avg,c,i}$	Average specific heat of hot/cold fluid across segment i	kJ/kg-°C
c_f	Cost per exergy unit-fuel	$/GJ
d_{eq}	Equivalent hydraulic diameter of recuperator channel	mm
$\dot{E}_{D,k}$	Exergy destruction rate-component k	kW
$\dot{E}_{q,k}$	Exergy rate due to heat transfer-component k	kW
$\dot{E}_{i,k}$, $\dot{E}_{o,k}$	Exergy rate at inlet, outlet-component k	kW
$\dot{E}_{P,k}$	Exergy product-component k	kW
$\dot{E}_{F,k}$	Exergy fuel-component k	kW
$\dot{E}_{L,k}$	Exergy loss-component k	kW
f_i	Friction coefficient-segment i	
f_k	Exergoeconomic factor	
$h_{c,i}$, $h_{c,o}$	Enthalpy at compressor inlet, outlet	kJ/kg
$h_{sc,o}$	Isentropic enthalpy at compressor outlet	kJ/kg
$h_{co,i}$	Enthalpy at combustor inlet	kJ/kg
$h_{t,i}$, $h_{t,o}$	Enthalpy at turbine inlet, outlet	kJ/kg
$h_{st,o}$	Isentropic enthalpy at turbine outlet	kJ/kg
$h_{ht,i}$/$h_{cd,i}$	Heat transfer coefficient of hot/cold fluid	kW/m^2-°C
k_p	Thermal conductivity of plate-recuperator	kW/m-°C
l_i	Length of segment	mm
$\dot{m}_{CO_2}$, $\dot{m}_{H_2O}$, $\dot{m}_{O_2}$, $\dot{m}_{CH_4}$, $\dot{m}_{rCO_2}$	Mass flow rate of CO_2, water-vapor, O_2, $\dot{m}_{CH_4}$, recycled CO_2	kg/s
Nu_i	Nusselt number through cold/hot segment i-recuperator	
N_{pairs}	Number of hot/cold channel pairs-recuperator	
n	Lifetime of plant	years
PR	Pressure ratio	
P_l, P_h	Pressure at compressor inlet, outlet	bar
Pr_i	Prandtl number through segment i	
P_{net}	Net power	kW
Q_i	Heat transfer from hot to cold fluid-segment i	kW
Q_{ph}	Heating load of preheater	kW
Re_i	Reynolds number through segment i	
S_r	Fraction of recycled sCO2 across LRT-HTR	
$T_{h,i}$, $T_{h,i+1}$	Temperature of hot fluid at inlet, outlet-segment i	°C
$T_{c,i}$, $T_{c,i+1}$	Temperature of cold fluid at inlet, outlet-segment i	°C
t_p	Thickness of each channel	mm
$\dot{W}_{t,a}$	Actual turbine power	kW
$\dot{W}_{c,a}$	Actual power consumed by compressor	kW

Greek

δ_{rel}	Relative roughness	
μ_i	Viscosity across segment i	kg/m-s
η_c η_t	Isentropic efficiency of compressor, turbine	
η_g	Conversion efficiency of generator	
η_{cycle}, $\eta_{overall}$	Thermal efficiency of cycle without-preheating, with-preheating	%
ρ_i	Density across segment i	kg/m^3
ε_k, ε_o	Second-law-efficiency of component k, cycle	%
ε_r	Effectiveness of recuperator	%
γ	Weighting coefficient	
τ	Annual operational time	hrs
ω	Interest rate	

LaPort. Heatric company developed the high-recuperative heat exchangers of this plant while Toshiba provides its turbine and combustor.

The numerous layouts of sCO_2 power cycles in open literature [28], try to improve the performance by improving cycle processes (heat addition, working-fluid expansion, regeneration, cooling, and compression processes) or by integrating the sCO_2 cycle with other systems [29]. The basic layout of sCO_2 cycle consists of compressor, heater, turbine, regenerator, and cooler. In the transcritical version, the gas compressor is replaced with liquid pump and the cooler is replaced with condenser. In the transcritical case, the lower pressure of the cycle is imposed by the condenser depending on the temperature of the cooling fluid (For instance: 32 °C for wet cooling and 50 °C for dry cooling). To overcome this limitation, the precompression process is involved. In the precompression cycle, an auxiliary compressor is used between the HTR and LTR to make the compressor inlet pressure independent from the turbine outlet pressure. This in turn make it possible to increase the lower pressure at the inlet of the condenser and to perform the condensation process at any available temperature of the cooling fluid. The regeneration process greatly affects the thermal efficiency of the CO_2 cycles [30]. Furthermore, there is significant difference between the physical properties of the sCO_2 of the hot (low pressure) and cold (high pressure) streams. Thus, the regeneration process is usually implemented by using two recuperators that operate at different range of temperatures to minimize the pinch point issue across the recuperators. The flow is different between the recuperators due to the physical properties of the sCO_2. However, some of the investigated layouts include only one [9,31], or without recuperator [28]. Similar to the improvements of the conventional Brayton cycle, the performance of the sCO_2 cycle can be enhanced by incorporating preheating of the recycled sCO_2 stream [24], reheating [32], multi-expansion [33], and intercooling compression processes [34]. However, the common shortcoming of these processes is addition of new components, which increases initial and maintenance costs and adds more complexity.

Exergoeconomic analysis combines, at the level of system components, thermodynamic evaluations based on an exergy analysis with economic principles. This is necessary to obtain useful information to the design and operation of a cost-effective system, but not obtainable by regular energy and economic analysis, which referred to as a thermoeconomic analysis. Furthermore, exergoeconomic analysis is a fundamental step to compare various options of the innovative cycles based on combined energetic, exergetic, and economic evaluations. Luo and Huang [8] investigated thermodynamic and exergoeconomic behavior of various sCO_2 power cycles for nuclear reactors. They have investigated six layouts including the simple recuperative, dual recuperative,

precompression, recompression, intercooling, and partial cooling cycles. Based on their thermal and cost-optimal designs, the simple recuperative cycle showed lowest efficiency and highest cost. The intercooling cycle showed better efficiency and comparable cost to that of partial cooling and recompression cycles. Liu et al. [35] proposed advanced exergoeconomic method to evaluate sCO2 recompression cycle. The advantages of the exergoeconomic analysis are the ability to determine the real potential for improvement of each significant component and to consider the interactions among components. Other researchers also evaluated the thermodynamic and exergoeconomic behavior of typical sCO_2 cycles integrated with other systems such as multi-effect desalination [36], power/cooling/heating [37,38], fuel cell [39], ORC [40,41], and geothermal [42].

As a significant improvement of the direct-fired oxy-combustion sCO_2 cycle, this paper is studying the effect of preheating process on the energetic and exergetic performances of the cycle in three layout configurations, not studied before. We propose the utilization and integration of preheater along with oxy-combustion and dry-cooler. In Allam cycle, the waste heat from the air separation unit (ASU) is proposed to be used to minimize the pinch-point problem of the LTR. Instead in this study, the preheating process of the recycled CO_2 is performed by external waste heat sources. It is performed by adding a preheater that receives part of the recycled sCO_2 by a split flow at the outlet of the compressor and connected in parallel with the LTR or in parallel with both the LTR and the HTR. In this way, the preheating process improves the cycle efficiency by minimizing the consumed fuel. Simultaneously, it improves the performance of recuperator by resolving the pinch point issue [43] as well as minimizing exergy destruction through recuperators [9]. Son et al. [44] presented preliminary performance estimation for integrated oxy-fuel sCO_2 cycle with concentrated solar power (CSP) focusing on reduction of fuel consumption. In summary, the main contributions of the present study are:

i) It is one of the first studies that investigates the direct oxy-combustion sCO_2 power cycle in terms of both thermodynamic and exergoeconomic analyses. Penkuhn and Tsatsaronis [45] reported exergy analysis of Allam cycle compared to similar oxy-combustion cycles and recommended further exergoeconomic and advanced exergy analysis frameworks to quantify potential improvements. Hervas and Petrakopoulou [46] introduced exergoeconomic analysis of the Allam cycle, however only at the design point of the original developers [47] without investigating the effects of the major operating conditions on the total product unit cost and the levelized cost of electricity.
ii) it proposes the utilization of the waste heat from external sources in different layout configurations to minimize the consumed fuel and to improve the cycle efficiency,
iii) it is the first study that investigates the performance of the direct oxy-fuel sCO_2 power cycle under dry-cooling conditions.

The present study is focusing on the preheating process with three layout configurations (M1, M2, and M3). The first configuration (M1) is the sCO_2 cycle without-preheater. The second configuration (M2) includes the preheater connected in parallel with low-temperature recuperator. The third configuration (M3) includes the preheater connected in parallel with both cycle recuperators (low and high-temperature recuperator). Furthermore, the analysis of the preheating process in this paper is performed within medium temperatures that are available from many external waste-heat sources. This thermodynamics and heat transfer study is necessary to optimize the operating conditions of the preheater in terms of split ratio, operating pressures, and the required temperature of heat source. Also, it specifies the optimum split ratio that yields the highest performance for cycle recuperators. Moreover, to elaborate on the contribution of the preheater in M2 and M3 to the improvement of the basic layout (M1), exergy and exergoeconomic analyses are applied to the three layout configurations and discussed thoroughly.

This study is presented in 4 main sections; the three layout configurations of the sCO_2 cycle are described in section 2. Section 3 introduces the energy, exergy, and exergoeconomic models with a discretized model for recuperator's calculations. The effect of split ratio on the performance, and the influence of the major parameters including the high- and low-cycle pressures, TIT, and compressor inlet temperature are investigated in section4. The sensitivity of exergy efficiency and total cost per unit exergy are discussed in section4.

2. Proposed sCO_2 cycle layouts

Referring to Fig. 1 (configuration M1), the major components of the direct oxy-fuel sCO_2 cycle are oxy-combustor, turbine, high-pressure recuperators, precooler, water separator, and compressor. For the combustion process, air-separation unit (ASU) equipped with a compressor produces pressurized oxygen (point 13). The high-pressure oxygen is mixed with the fuel (methane point 12) and combusted in the combustor. The high-temperature combustion products are diluted by the recycled CO_2 (state 11). The combustion products enter the turbine at high temperature and pressure (state 1). By the expansion process, the gas turbine converts the enthalpy energy to electrical energy. Also, part of the produced power is used to drive the compressor, dry cooling unit, and ASU (parasitic power). The turbine exhausts proceed to the high-temperature recuperator (HTR, state 2 to 3) then to the low-temperature recuperator (LTR, state 3 to 4). After the recuperation process, the working fluid is cooled in the pre-cooler to near-critical state (state 6). At this state, the water content is separated from the working fluid in the water separator and the pure CO_2 is compressed to the high-pressure of the cycle. Before the compression process, part of the sCO_2 is exported at a rate equals the rate of the CO_2 produced by the combustion process (to maintain constant mass flow rate). The other part is compressed and recycled to the combustion process after being heated by the LTR and HTR. Fig. 2 (configuration M2) and Fig. 3 (configuration M3) represent the same system with the addition of a preheater to the cycle. The preheater can be connected in parallel with the LTR as in Fig. 2 or parallel with both recuperators as in Fig. 3. Even though the preheater is an additional component to the layout, it significantly improves the cycle efficiency of the system (explained later). The preheater can be driven by utilizing free waste heat or renewable sources. Also, splitting the flow at the compressor outlet presents a way to resolve the pinch-point issue of the recuperators. It is similar to the effect of the split flow investigated in Ref. [43]. Furthermore, the design point of the present cycle considers moderate TIT (750 °C) to reduce thermal stresses associated with high TIT.

3. Energy and exergy models

To investigate the effect of the preheating process within the basic layout of the direct oxy-fuel sCO_2 cycle (M1), a comprehensive and rigorous thermodynamics and heat transfer model is developed and validated to simulate 50MWe sCO_2 power plant. The model assumptions are:

- Pressure drops through combustor, water separator, and pipes are neglected [8].

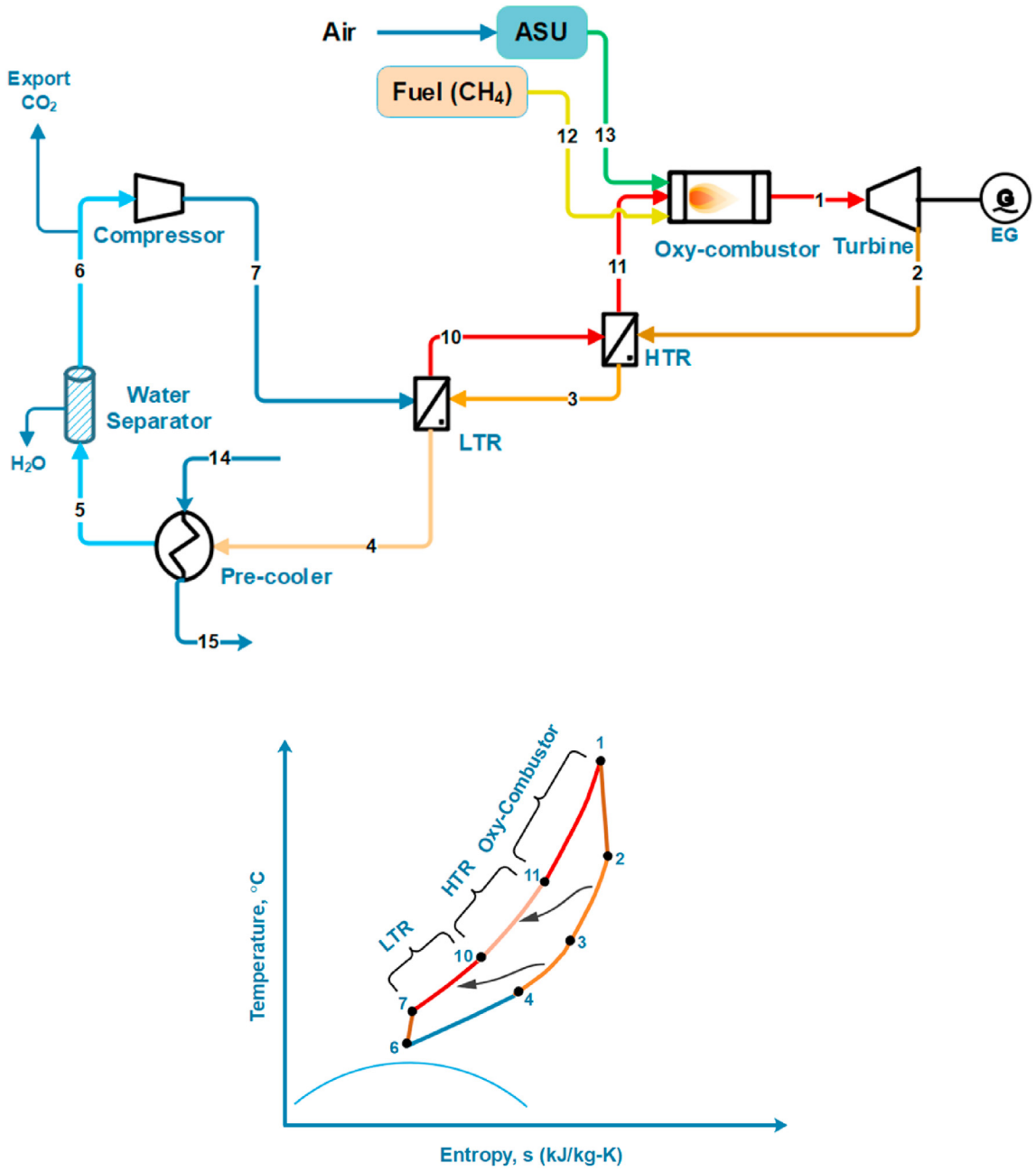

Fig. 1. Schematic layout and T-S diagram of direct oxy-fuel sCO_2 cycle without-preheater (M1).

- Pressure drops across recuperators, preheater, and precooler do not exceed 5% of the inlet pressure [8].
- Heat losses from components to ambient air are neglected.
- For M2 and M3, the preheater is always available when full electric output is demanded. If the preheating source is not available, the cycle can work as configuration M1. However, in this case, the heat recovery amount by the recuperators of M2 and M3 will be less than in M1. Therefore, more fuel must be supplied to the combustor to provide the design output of the cycle.

3.1. Energy model

To minimize the consumed power by the compressor, the excess sCO_2 is exported before the compression process as shown in Fig. 1. To make this possible, the outlet pressure of the turbine is set in the range of 78 bar−110 bar to achieve a relatively high pressure at the inlet of the compressor (75 bar−105 bar) which are recommended for CO_2 exportation [48,49]. The compressor in Figs. 1–3 is directly driven by the turbine and the consumed power for the compression process is given as:

$$\dot{W}_{c,a} = \dot{m}_{rCO_2}\left(h_{sc,o} - h_{c,i}\right)_{rCO_2} \Big/ \eta_c \tag{1}$$

where $\dot{m}_{rCO2}$ is the mass flow rate of recycled sCO_2. $h_{sc,o}$, $h_{c,i}$ Are isentropic enthalpies at the outlet and inlet of the compressor, respectively. η_c is compressor isentropic efficiency.

Designating the target electrical power of the cycle as P_{net}, the

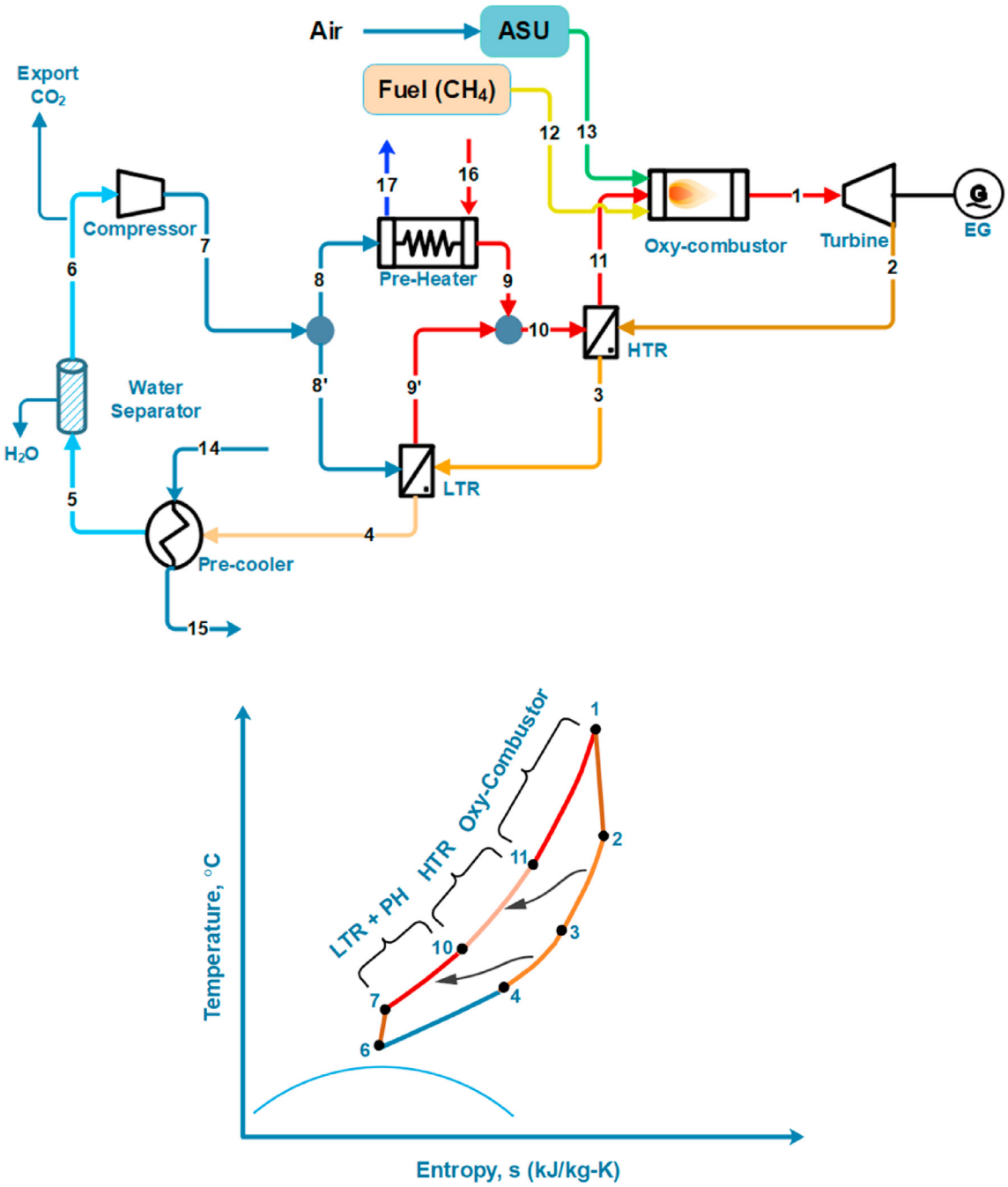

Fig. 2. Schematic layout and T-S diagram of direct oxy-fuel sCO_2 cycle with-preheater connected in parallel with LTR (M2).

generator efficiency as η_g, and the actual work of the turbine as $\dot{W}_{t,a}$, the net power produced by the turbine [8]:

$$P_{net} = \left(\dot{W}_{t,a} - \dot{W}_{c,a}\right) \Big/ \eta_g \tag{2}$$

In terms of the isentropic efficiency and enthalpies at turbine inlet and outlet with a mass flow rate of the combustion products, the actual turbine power [50]:

$$\dot{W}_{t,a} = \eta_t \times \left\{ \dot{m}_{CO_2} \left[h_{t,i} - h_{st,o}\right]_{CO_2} + \dot{m}_{H_2O} \left[h_{t,i} - h_{st,o}\right]_{H_2O} \right\} \tag{3}$$

where $h_{t,i}$ is turbine inlet enthalpy, $h_{st,o}$ is the isentropic enthalpy at outlet of the turbine, (which is obtained at the outlet pressure of the turbine and specific entropy equals to the specific entropy of the same fluid at the inlet of the turbine), $\dot{m}_{CO_2}$ and $\dot{m}_{H_2O}$ are mass flow rates of CO_2 and water steam leaving the combustor, and η_t is turbine isentropic efficiency.

The actual combustion in the combustor:

$$CH_4 + CO_2 + 2O_2 \rightarrow 2CO_2 + 2\,H_2O \tag{4}$$

Applying energy and mass conservation principles on the combustor, the mass flow rates of the required oxygen and recycled CO_2 could be obtained to satisfy pre-specified conditions at turbine

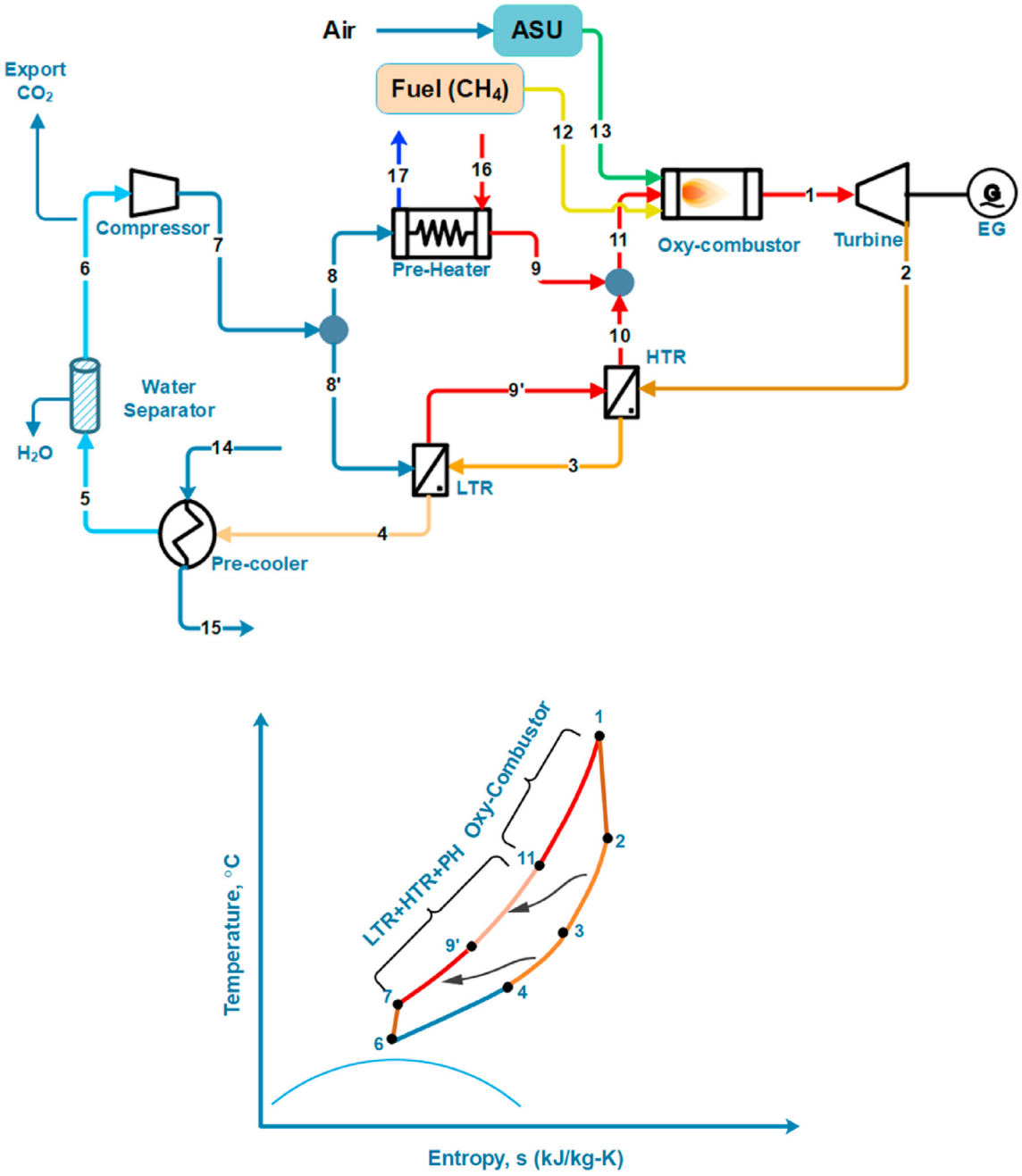

Fig. 3. Schematic layouts and T-S diagram of direct oxy-fuel sCO_2 cycle with-preheater connected in parallel with both LTR and HTR (M3).

inlet. The conservation of mass across the combustor:

$$\dot{m}_{O_2} + \dot{m}_{CH_4} + \dot{m}_{rCO_2} = \dot{m}_{CO_2} + \dot{m}_{H_2O} \tag{5}$$

And the conservation of energy:

$$\dot{m}_{O_2}\,[h_{co,i}]_{O_2} + \dot{m}_{CH_4}\,[h_{co,i}]_{CH_4} + \dot{m}_{rCO_2}\,[h_{co,i}]_{rCO_2} = \dot{m}_{CO_2}\,[h_{t,i}]_{CO_2} + \dot{m}_{H_2O}\,[h_{t,i}]_{H_2O} \tag{6}$$

It should be note that $[h_{co,i}]_{CH_4}$ includes both the sensible and the heating value of the fuel. From Eq. (4), it can be noted that 2 kmol of oxygen is needed for each kmol of the fuel. The molar weight of the oxygen is 32 kg/kmol and the molar weight of the fuel (CH_4) is 16 kg/kmol. So, it can be noted that 64 kg of oxygen is needed for each 16 kg of the fuel. In mathematical form, the required mass flow rate of the oxygen must be four times the mass flow rate of fuel as shown in Eq. (7). In the ideal combustion (without recycled CO_2), each kmol of the combusted fuel produce 1 kmol of the carbon dioxide (CO_2), which has a molecular weight of 44 kg/kmol. That is to say that each 16 kg of the fuel produces 44 kg of CO_2, which is 2.75 higher than the mass of the fuel. So, the recycled CO_2 is equal to the total CO2 at the outlet of the combustor minus the new produced CO_2 in the combustor ($\dot{m}_{new,\,CO_2} = 2.75\,\dot{m}_{CH_4}$) as expressed in Eq. (8).

$$\dot{m}_{O_2} = 4\,\dot{m}_{CH_4} \tag{7}$$

$$\dot{m}_{rCO_2} = \dot{m}_{CO_2} - 2.75\,\dot{m}_{CH_4} \tag{8}$$

Let Q_{ph} be the heat absorbed by the preheater from an external waste heat resource. For M1, $Q_{ph} = 0$, while for M2 and M3 is given in Eqs. (9) and (10):

$$Q_{ph,\,M2} = \dot{m}_{rCO_2}(1 - S_r)[h_{10} - h_7]_{rCO_2} \tag{9}$$

$$Q_{ph,\,M3} = \dot{m}_{rCO_2}(1 - S_r)[h_{11} - h_7]_{rCO_2} \tag{10}$$

Without considering the preheating load (assuming it is available from free sou rce), the efficiency of the cycle is:

$$\eta_{cycle} = \frac{P_{net}}{\dot{m}_{CH_4} \times LHV} \tag{11}$$

While the overall efficiency of the cycle (including the pre-heating load) is:

$$\eta_{overall} = \frac{P_{net}}{Q_{ph} + \dot{m}_f \times LHV} \tag{12}$$

where $\dot{m}_f = \dot{m}_{CH_4}$.

3.2. Discretized model of recuperators, pre-heater, and precooler

Due to its compactness and high effectiveness, the printed circuit heat exchanger (PCHE) is selected for the recuperators and precooler of the sCO_2 cycles [51,52]. It consists of alternately cold and hot flow channels, Fig. 5(a and b). Since the specific heat of the sCO2 changes dramatically near critical and pseudo-critical points (or at high pressures with low temperatures, see Fig. 4), the heat exchanger unit is divided into N segments (with equal lenghs) along flow direction to obtain precise output temperatures. Assuming uniform flow, a single pair (Fig. 5(b)) of the channels can be modeled as a heat exchanger and the heat transfer across each segment is:

$$Q_i = U_{o,i} A_{o,i} \Delta T_i \tag{13}$$

where $U_{o,i}$ is segment overall heat transfer coefficient, $A_{o,i}$ is the heat transfer area between hot and cold channels, and ΔT_i is the log-mean temperature difference across each segment:

$$\Delta T_i = \frac{(T_{h,i+1} - T_{c,i+1}) - (T_{h,i} - T_{c,i})}{\ln\left(\frac{T_{h,i+1} - T_{c,i+1}}{T_{h,i} - T_{c,i}}\right)} \tag{14}$$

and $U_{o,i}$ is:

$$U_{o,i} = \frac{1}{\frac{1}{h_{ht,i}} + \frac{1}{h_{cd,i}} + \frac{t_p}{k_p}} \tag{15}$$

where $h_{ht,i}$ and $h_{cd,i}$ are the heat transfer coefficients between the hot/cold flow and the plate in each channel pair, respectively. For turbulent flow, these coefficients are obtained from the Gnielinski empirical Nusselt number correlation [53] and verified by Serrano et al. [54] for straight semi-circular channels:

$$Nu_i = \frac{\left(\frac{f_c}{8}\right)(Re_i - 1000)\cdot Pr_i}{1 + 12.7\cdot\left(Pr_i^{2/3} - 1\right)\cdot\sqrt{f_{c,i}/8}}, \quad 5000 \le Re \le 5\times 10^6, \mathrm{Pr} = 0.5 \sim 2000 \tag{16}$$

$$f_{c,i} = \left(\frac{1}{1.8\log Re_i - 1.5}\right)^2 \tag{17}$$

$$Re_i = \frac{4\,\dot{m}_i}{\pi \mu_i d_{eq}} \tag{18}$$

where d_{eq} is the equivalent hydraulic diameter of the semi-circular channel:

$$d_{eq} = \frac{4\pi d^2}{8\cdot\left(\frac{\pi}{2}d + d\right)} \tag{19}$$

For laminar flow conditions ($Re < 2300$), the Nusselt number is

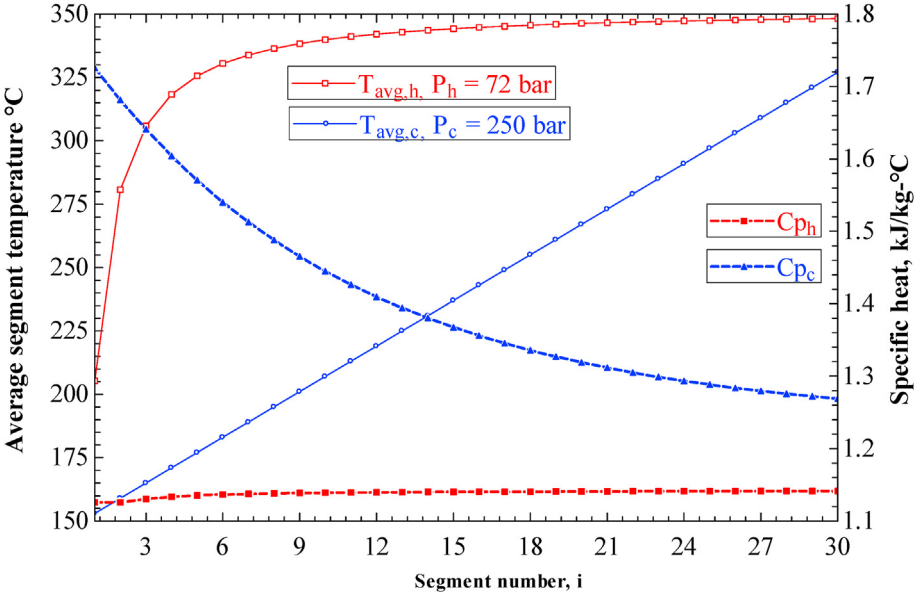

Fig. 4. Variation of sCO2 specific heat along segments of typical LTR at $P_h = 250$ bar, $P_l = 75$ bar, $T_{h,in} = 350$ °C, and $T_{c,in} = 150$ °C. Note: the segments are assumed to have the same length.

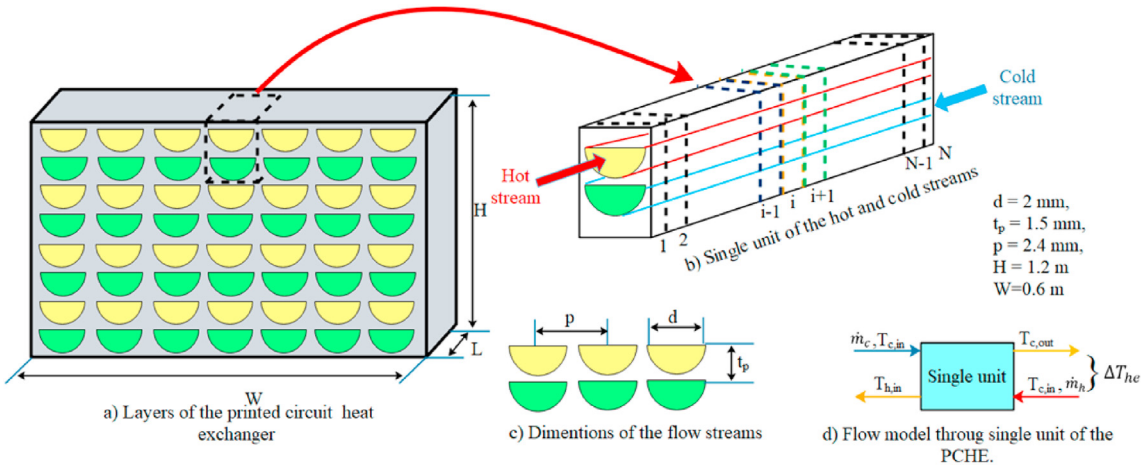

Fig. 5. Discretized model of PCHE.

constant and fixed as $Nu_i = 4.089$. The mass flow rate ($\dot{m}$) in each hot and cold channel is:

$$\dot{m}_{h,i} = \frac{\dot{m}_{hot}}{N_{pairs}}, \quad \dot{m}_{c,i} = \frac{\dot{m}_{cold}}{N_{pairs}} \tag{20}$$

where $\dot{m}_{hot}$ and $\dot{m}_{cold}$ are the total mass flow rates of the hot and cold steams.

For each single heat exchanger unit (as shown in Fig. 5 (b)) the total number of the segments (N) was iteratively selected until the total pressure drop does not exceed 5% of the inlet pressure. The total pressure drop (in hot or cold sides):

$$\Delta P_{total} = \sum_{i=1}^{N} \Delta P_i \tag{21}$$

$$\Delta P_i = f_i \cdot \frac{l_i}{d_{eq}} \cdot \rho_i \frac{V_i^2}{2} \tag{22}$$

where f_i is the friction factor. For turbulent flow [8]:

where δ_{rel} is the relative roughness:

$$f_i = 0.11 \cdot 441.19\delta_{rel}^{-1.1772}\Big)\Big(441.19\delta_{rel}^{-1.1772}\Big)\Big(441.19\delta_{rel}^{-1.1772}\Big)^{-1}\Big)^{0.25} \tag{23}$$

$$\delta_{rel} = e/d \tag{24}$$

Length of each segment l_i is estimated until ($\Delta P_{total} \leq 5\%$ of the inlet pressure).

The heat transfer across each segment is substituted in terms of the temperature difference of the hot and cold stream as follows:

$$Q_i = \dot{m}_{h,i} \cdot cp_{avg,h,i} \cdot \Delta T_{h,i}, \quad \Delta T_{h,i} = T_{h,i+1} - T_{h,i} \tag{25}$$

$$Q_i = \dot{m}_{c,i} \cdot cp_{avg,c,i} \cdot \Delta T_{c,i}, \quad \Delta T_{c,i} = T_{c,i+1} - T_{c,i} \tag{26}$$

Once l_i and the total length of all segments are determined, Eqs. (13), (25) and (26) are solved simultaneously to obtain the hot and cold temperatures.

3.3. Exergy model

After solving the energy model and obtaining temperatures and pressures at each state, the total exergy and the physical exergy are calculated:

$$\dot{E} = \dot{E}_{ph} + \dot{E}_{ch} \tag{27}$$

$$\dot{E}_{ph} = \dot{m}[(h - h_o) - T_o(s - s_o)] \tag{28}$$

Exergy balance for component k is used to obtain its exergy destruction rate $\dot{E}_{D,k}$ [45]:

$$\dot{E}_{D,k} = \sum_j \dot{E}_{q,k} + \dot{W}_k + \sum_i \dot{E}_{i,k} - \sum_o \dot{E}_{o,k} \tag{29}$$

For each cycle component, the exergy efficiency is expressed in terms of the fuel exergy ($\dot{E}_{F,k}$) and product exergy ($\dot{E}_{P,k}$) of the component as given in Eq. (30):

$$\varepsilon_k = \frac{\dot{E}_{P,k}}{\dot{E}_{F,k}} \tag{30}$$

For the overall system analysis, exergy loss to the environment ($\dot{E}_{L,k}$) must be considered such that the overall second law efficiency is:

$$\varepsilon_o = \frac{\sum \dot{E}_{P,k}}{\sum \dot{E}_{F,k}} = 1 - \frac{\sum\left(\dot{E}_{D,k} + \dot{E}_{L,k}\right)}{\sum \dot{E}_{F,k}} \tag{31}$$

Table 1 shows the definitions of $\dot{E}_{F,k}$, $\dot{E}_{P,k}$, $\dot{E}_{D,k}$, and $\dot{E}_{L,k}$ for M1.

Table 1
Definitions of fuel, product, destruction, and loss exergies for components of M1.

Component	$\dot{E}_{F,k}$	$\dot{E}_{P,k}$,	$\dot{E}_{D,k}$	$\dot{E}_{L,k}$
Oxy-combustor	$\dot{E}_{11}+\dot{E}_{12}+\dot{E}_{13}$	$\dot{E}_1$	$\dot{E}_{11}+\dot{E}_{12}+\dot{E}_{13}-\dot{E}_1$	0
Turbine	$\dot{E}_1-\dot{E}_2$	$\dot{W}_{t,a}$	$\dot{E}_1-\dot{E}_2-\dot{W}_{t,a}$	0
Compressor	$\dot{W}_{c,a}$	$\dot{E}_7-\dot{E}_6$	$\dot{W}_{c,a}-(\dot{E}_7-\dot{E}_6)$	0
HTR	$\dot{E}_2-\dot{E}_3$	$\dot{E}_{11}-\dot{E}_{10}$	$\dot{E}_2-\dot{E}_3-(\dot{E}_{11}-\dot{E}_{10})$	0
LTR	$\dot{E}_3-\dot{E}_4$	$\dot{E}_{10}-\dot{E}_7$	$\dot{E}_3-\dot{E}_4-(\dot{E}_{10}-\dot{E}_7)$	0
Preheater	$\dot{E}_{16}-\dot{E}_{17}$	$\dot{E}_9-\dot{E}_8$	$\dot{E}_{16}-\dot{E}_{17}-(\dot{E}_9-\dot{E}_8)$	0
Precooler	$\dot{E}_4$	$\dot{E}_5$	$\dot{E}_4-\dot{E}_5$-$(\dot{E}_{15}-\dot{E}_{14})$	$\dot{E}_{15}-\dot{E}_{14}$

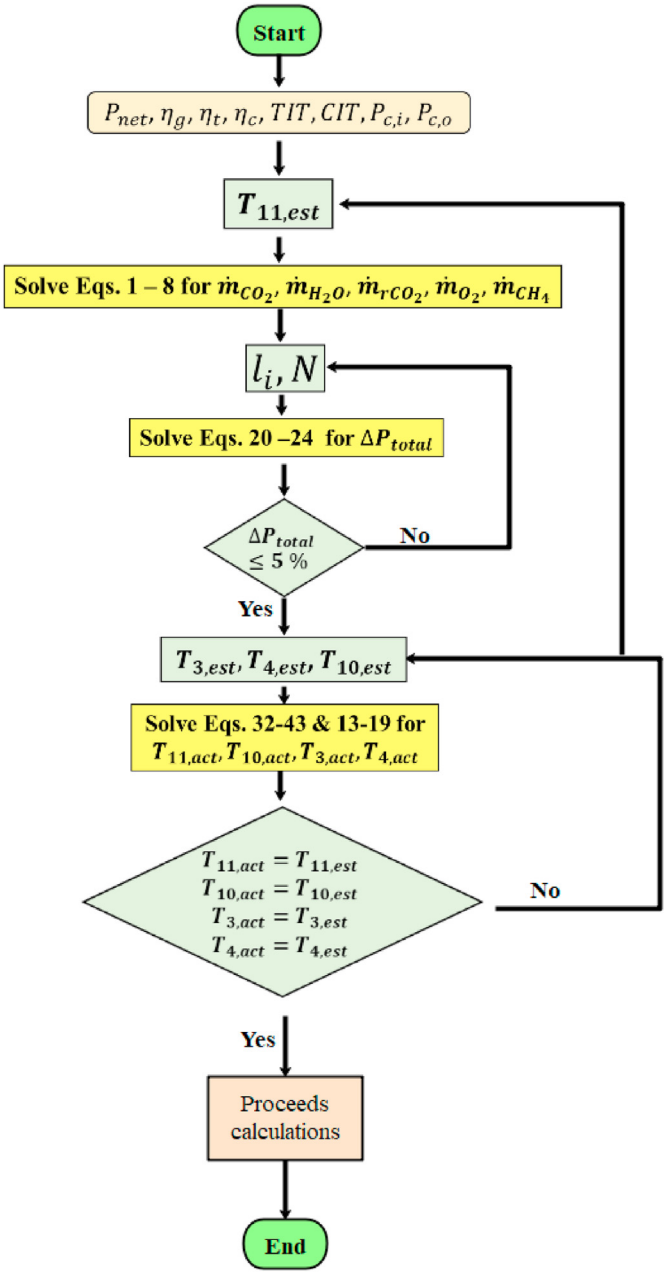

Fig. 6. Flow chart and calculation procedures.

3.4. Algorithm flow chart

To simulate the performance of preheater in M2 and M3 configurations, the calculation procedures (as shown in Fig. 6) are performed as follows: first, thermodynamics code is written to obtain the thermodynamics properties of sCO_2 at the specified states and to solve the model equations simultaneously (using the Engineering Equation Solver (EES) program). The input parameters are varied one at a time within the specified range shown in Table 2. The solver automatically obtains the thermodynamics data based on the relations (Fig. 5) and specific heats at pre-assumed average temperatures of each segment. The code solves the unknowns (T_3, T_4, T_{10}, and T_{11}) and calculates the actual average temperatures of each segment of the recuperators. Then, the average calculated temperatures are compared to the pre-assumed ones and the calculation process is repeated using the new average temperatures as inputs for the next iteration until convergence.

Table 2
Input parameters of the direct oxy-fuel preheated sCO2 cycle.

Parameter	Range	Design value
Higher pressure P_h[bar]	200–300	250
Lower pressure P_l[bar]	75–100	78
Turbine inlet temperature, T_{max}[°C]	500–800	750
Compressor inlet temperature, T_{min}[°C]	33–50	50
Split ratio, S_r	0.2–1	0.5
Net electrical power, P_{net}[MW]	50	50
Efficiency of generator, η_g[%]	95	95
Efficiency of turbine, η_t[%]	90	90
Efficiency of compressor, η_c[%]	85	85
LHV-methane[kJ/kg]	50,050	50,050
Power consumed by the air separation unit, MW	6.5	6.5

The pre-assumed temperatures are predicted as following:

1) guess the outlet temperatures of the hot and cold streams ($T_{3,est}$, $T_{4,est}$, $T_{10,est}$, $T_{11,est}$), l_i and N.
2) assume uniform temperature difference in hot and cold streams such that the initial guess:

$$\Delta T_{i,\ h,\ HTR\_est} = \frac{T_2 - T_{3,est}}{N}, \tag{32}$$

$$\Delta T_{i,\ h,\ LTR\_est} = \frac{T_{3,est} - T_{4,est}}{N}, \tag{33}$$

$$\Delta T_{i,\ c,\ HTR\_est} = \frac{T_{11,est} - T_{10,est}}{N} \tag{34}$$

$$\Delta T_{i,\ c,\ LTR\_est} = \frac{T_{10,est} - T_7}{n} \tag{35}$$

3) calculate the average temperature of each segment based on assumed values in 1 and 2 as:

Table 3
Cost balance and auxiliary equations of M1.

Components	Cost balance	Auxiliary
Oxy-combustor	$\dot{C}_1 = \dot{C}_{11} + \dot{C}_{12} + \dot{C}_{13} + \dot{Z}_{oc}$	Nil
Turbine	$\dot{C}_2 + \dot{C}_{p,t} = \dot{C}_1 + \dot{Z}_t$	$\frac{\dot{C}_1}{\dot{E}_1} = \frac{\dot{C}_2}{\dot{E}_2}$
Compressor	$\dot{C}_7 - \dot{C}_{p,c} = \dot{C}_6 + \dot{Z}_c$	$\frac{\dot{C}_{p,t}}{\dot{W}_{t,a}} = \frac{\dot{C}_{p,c}}{\dot{W}_{c,a}}$,
HTR	$\dot{C}_{11} + \dot{C}_3 = \dot{C}_2 + \dot{C}_{10} + \dot{Z}_{HTR}$	$\frac{\dot{C}_2}{\dot{E}_2} = \frac{\dot{C}_3}{\dot{E}_3}$
LTR	$\dot{C}_{10} + \dot{C}_4 = \dot{C}_3 + \dot{C}_7 + \dot{Z}_{LTR}$	$\frac{\dot{C}_3}{\dot{E}_3} = \frac{\dot{C}_4}{\dot{E}_4}$,
Preheater	$\dot{C}_9 + \dot{C}_{17} = \dot{C}_8 + \dot{C}_{16} + \dot{Z}_{ph}$	$\frac{\dot{C}_8}{\dot{E}_8} = \frac{\dot{C}_9}{\dot{E}_9}$
Precooler	$\dot{C}_{14} + \dot{C}_6 = \dot{C}_4 + \dot{C}_{15} + \dot{Z}_{pc}$	$\frac{\dot{C}_4}{\dot{E}_4} = \frac{\dot{C}_6}{\dot{E}_6}$, $\dot{C}_{14} = 0$

$$T_{i,c,avg,\ LTR} = T_7 + \Delta T_{i,\ c,\ LTR\_est} \times (i - 0.5), \tag{36}$$

$$T_{i,c,avg,\ HTR} = T_{10,est} + \Delta T_{i,\ c,\ HTR\_est} \times (i - 0.5), \tag{37}$$

$$T_{i,h,avg,\ HTR\_est} = T_2 - \Delta T_{i,\ h,\ HTR\_est} \times (N/i - 0.5), \tag{38}$$

$$T_{i,h,avg,\ LTR\_est} = T_{3,est} - \Delta T_{i,\ h,\ LTR} \times (N/i - 0.5) \tag{39}$$

4) solve pressure drop equations 21–24 until the total number of hot/cold channels and the length of each segment $l_i$satisfy the pressure drop criteria ($\Delta P_{total} \leq 5\%$ of the inlet pressure).
5) solve Eqs. (1)–(19) with Eqs.(25) and (26) simultaneously to obtain the actual temperature difference of recuperator segments and calculate actual outlet temperatures as:

$$T_{3,act} = T_2 - \sum_{i=1}^{N} \Delta T_{i,h,\ HTR\_act}, \tag{40}$$

$$T_{4,act} = T_{3,act} - \sum_{i=1}^{N} \Delta T_{i,h,\ LTR\_act}, \tag{41}$$

$$T_{10,act} = T_7 + \sum_{i=1}^{N} \Delta T_{i,c,\ LTR\_act}, \tag{42}$$

$$T_{11,act} = T_{10,act} + \sum_{i=1}^{N} \Delta T_{i,c,\ HTR\_act}, \tag{43}$$

6) compare actual and estimated temperatures, repeat until convergence.

The design input parameters are shown in Table 2 with cycle high-pressure range from 200 to 300 bar. The high-pressure is one of the challenges of sCO_2 technology, however, Heatric company developed high-pressure recuperators (PCHEs) fabricated from 617 alloy and able to operate at 300 bar [27]. To make a purely supercritical analysis, the lowest values of the temperature and pressure at the compressor inlet are specified to be higher than the critical point of the CO_2 (31 °C, 73.8 bar), while the highest values are selected based on dry-cooling conditions. The turbine and compressor isentropic efficiencies were selected based on available data in literature. To be conservative, the effectiveness of recuperators was set less than reported values in literature. Moreover, the power consumed by the air separation unit (ASU) was taken as 13% from the net output power of the cycle as recommended by Allam et al. [27].

3.5. Exergoeconomic model

Exergoeconomic analysis combines exergy and economic analyses at the level of the system components [36]. In this study, the exergoeconomic model is built to obtain product cost per unit exergy. The contribution of each component in the final product cost is used to evaluate the effects of including preheater and split process at the compressor exit. The general cost balance equation is applied to each component to obtain the cost rate of each stream:

$$\sum \dot{C}_{out,k} + \dot{C}_{po,k} = \sum \dot{C}_{in,k} + \dot{C}_{q,k} + \dot{Z}_k \tag{44}$$

where $\dot{C}_{in,k}$ and $\dot{C}_{out,k}$ are the cost rates of inlet and outlet streams of the component. $\dot{C}_{q,k}$ and $\dot{C}_{po,k}$ are the cost rates related to the thermal energy input and power output of the component (if

Table 4
Equipment cost formulae (baselined to 2019 U S. dollars using the average Chemical Engineering Plant Cost Index (CEPCI) for 2019, the last full year for which CEPCI values were available for this study [56]).

Component	Capital investment cost	Original application	Notes
Oxy-combustor	$Z_{oc} = 677203 \times Q_{oc}^{0.6} \times f_{T,oc}$ $f_{T,oc} = 1 + 5.4 \times 10^{-5}(T_{max} - 550)^2$	Natural gas-fired primary heaters	Q_{oc} in MW
Turbine	$Z_t = 195382 \times \dot{W}_{t,a}^{0.5561} \times f_{T,t}$ $f_{T,t} = 1 + 1.106 \times 10^{-4}(T_{max} - 550)^2$	Axial turbine	$\dot{W}_{t,a}$ in MW
Compressor	$Z_c = 1316100 \times \dot{W}_{c,a}^{0.3992}$	Integrally geared centrifugal compressor	$\dot{W}_{c,a}$ in MW
HTR	$Z_{HTR} = 52.91 \times (UA)_{HTR}^{0.7544} \times f_{T,\ HTR}$ $f_{T,\ HTR} = 1 + 0.02141\ (T_{max} - 550)$	PCHE	UA in W/°C
LTR	$Z_{LTR} = 52.91 \times (UA)_{LTR}^{0.7544} \times f_{T,\ LTR}$ $f_{T,\ LTR} = 1 + 0.02141\ (T_{max} - 550)$	PCHE	UA in W/°C
Preheater	$Z_{ph} = 52.91 \times (UA)_{ph}^{0.7544} \times f_{T,\ ph}$ $f_{T,\ HTR} = 1 + 0.02141\ (T_{max} - 550)$	PCHE	UA in W/°C
Precooler [8]	$Z_{pc} = 35.18 \times (UA)_{pc}^{0.75}$	Direct air cooler	UA in W/°C

Table 5
Comparison between oxy-combustion sCO_2 power systems.

System	Classification	Compression	Regeneration	Heat source	Expansion	Design conditions	Thermal efficiency(%)
Allam [27]	Single-flow	Gas compressors + intercooler + condenser +liquidpump	Single-recuperator	Single Oxy-combustor	Single-expander	P_h = 300 [bar] P_l = 30 [bar] T_{max} = 1150 [°C] T_{min} = 20 [°C]	59.0
Allam + RH [27]	Single-flow	Gas compressors + intercooler + condenser +liquidpump	Single-recuperator	Oxy-combustor + reheater	Dual-expanders	P_h = 300 [bar] P_l = 1 [bar] T_{max} = 1150 [°C] T_{min} = 20 [°C]	60.0
Matiant [58]	Single-flow	Gas compressor + intercoolers	Single-recuperator	Oxy-combustor + reheater	Dual-expanders	P_h = 300 [bar] P_l = 1 [bar] T_{max} = 1300 [°C] T_{min} = 29 [°C]	44.3
DEMO [59]	Single-flow	Gas compressors + intercooler + condenser +liquidpump	Single-recuperator	Oxy-combustor + reheater	Triple-expanders	P_h = 240 [bar] P_l = 4 [bar] T_{max} = 1250 [°C] T_{min} = 20 [°C]	52.0
Recuperated CPOC [60]	Single-flow	Gas compressors + intercooler + condenser +liquidpump	Dual-recuperator	Single Oxy-combustor	Single-expander	P_h = 175 [bar] P_l = 1 [bar] T_{max} = 1150 [°C] T_{min} = − 62.0 [°C]	63.0
Quasi Combined [61]	Split-flow before compression	Gas compressor + condenser + liquidpump	Dual-recuperator	Single Oxy-combustor	Dual-expanders	P_h = 156 [bar] P_l = 1 [bar] T_{max} = 1300 [°C] T_{min} = − 70 [°C]	65.6
CPOC [60]	Single-flow	Gas compressor + condenser + liquidpump	No-recuperator	Single Oxy-combustor	Single-expander	P_h = 152 [bar] P_l = 1 [bar] T_{max} = 530 [°C] T_{min} = − 17.7 [°C]	30.0
TCO [62]	Single-flow	Gas-compressor + condenser + liquidpump	Dual-recuperator	Oxy-combustor + reheater	Dual-expander	P_h = 483 [bar] P_l = 1 [bar] T_{max} = 705 [°C] T_{min} = 20 [°C]	40.0
Present study	Split-flow before recuperator/preheating	Gas-compressor	Dual-recuperator	Pre-heater + Oxy-combustor	Single-expander	P_h = 250 [bar] P_l = 75 [bar] T_{max} = 750 [°C] T_{min} = 50 [°C]	41.67(M1) 46.07(M2) 53.04(M3)

existed). $\dot{Z}_k$ is the sum of capital investment, maintenance, and operating costs, which is expressed as in Eq. (45) [37]. Table 3 shows the application of Eq. (44) on each component of M1.

$$\dot{Z}_k = \left(\frac{CRF}{\tau}\right) Z_k + \gamma_k Z_k \Big/ \tau \tag{45}$$

where Z_k is the total investment, operating, and maintenance costs of each component which is presented in Table 4. γ_k is the

weighting coefficient (fixed at 0.06) and τ is the plant operation time per year (8000 h). The *CRF* is the capital recovery factor which is related to the interest rate ($\omega = 12\%$) and the lifetime of the plant ($n = 20\ years$):

$$CRF = \frac{\omega \cdot (1+\omega)^n}{(1+\omega)^n - 1} \tag{46}$$

Two indicators are used to evaluate the exergoeconomic performance of the system; the total product unit cost ($c_{P,total}$):

$$c_{P,total} = \frac{\sum_{i=1}^{n_k} \dot{Z}_k + \sum_{i=1}^{n_f} c_f \dot{E}_F}{\sum_{i=1}^{n_p} \dot{E}_P} \tag{47}$$

and the exergyeconomic factor f_k [55]:

$$f_k = \frac{\dot{Z}_k}{\dot{Z}_k + \dot{C}_{D,k}} \tag{48}$$

where $\dot{C}_{D,k} = c_{F,k}\dot{E}_{D,k}$

The equipment cost formulae in Table 4 are obtained from Nathan et al. comprehensive study [57] which were baselined to 2017 U S. dollars using the average Chemical Engineering Plant Cost Index (CEPCI) for 2017. These correlations were built based on various vendor quotes and adjusted for two independent sources of uncertainty, which are: 1) vendor quote confidence rating uncertainty, and 2) cost model weighted correlation error (how well the model fits the vendor data). Furthermore, the developed correlations by Nathan et al. [57] include temperature correction factor to account for material selection as a function of temperature. In this study, the costs are translated to 2019 U S. dollars by multiplying the original correlation from Ref. [57] by the ratio of the average CEPCI index for 2019 (607.5) [56] to the average CEPCI index for 2017 (567.5) [57]. It worth mentioning that the difference between the results of the cost formulae used in this study and those used by Luo and Huang [8], which were developed based on old year indexes (between 1986 and 2003) is about 6.64% in the resulted total product unit costs that were presented in section 4.7.

4. Results and discussion

4.1. Comparison and validation

Table 5 presents comparison between the present work and the previously published studies that use oxy-combustor to heat the sCO_2 to the desired TIT. It can be noted that the available previous studies include oxy-combustor only or with addition of a reheater, while the integration of the preheater and oxy-combustor, presented in the present study is not available in literature. Considering the compression process, almost all listed studies use the intercooling compression in combination with a liquid pump. This implies that the compression process takes place near or below the critical state and the wet cooling method is involved. However, wet cooling is not always available and requires considerable amount of water and large area. So, in the present study, dry cooling is selected to cool the working fluid up to a minimum temperature of 50 °C. Looking at the thermal efficiency of these studies, it is mainly related to the pressure and temperature at the inlet of the turbine and the compressor. The quasi-combined and the recuperated Cryogenic Pressurized Oxy-Combustion (CPOC) cycles have thermal efficiencies of 65.6% and 63%, respectively. Even though these cycles have very high efficiencies, they are impractical cycles due to their layout complexity, high rated TIT, and cryogenic cooling system. The efficiency of the CPOC cycle without recuperator and with moderate TIT is about 30% with a simpler layout. The basic Allam cycle and Allam cycle with the reheating process have efficiencies (at same design conditions) of about 59% and 60%, respectively. The very high pressure of the Allam cycle (300 bar) and low minimum temperature (20 °C) with high TIT (1150 °C) yield slightly higher efficiency than the proposed one in this work. In this study, to avoid technical issues associated with the high pressures and high TIT, a pressure of 250 bar and temperature of (750 °C) were set at the turbine inlet (state 1) with an achievable minimum temperature of

Table 7
Specification of two waste heat sources that have a major potential to drive the preheater proposed in M2 and M3[a].

Heat source #	S1 [65]	S2 [66]
Source type	MGT	GTC
HTF	EGM	EGM
T_{16}, °C	554	680
ΔT_{ph}, °C	20	20
$\dot{m}_{ph}$, kg/s	89	178

[a] HTF: heat transfer fluid; MGT: marine gas turbine; GTC: gas turbine cycle; EGM: exhaust gas mixture.

Table 6
Comparison of the model results with data given by Refs. [63,64].

Parameter	Ref. [63]	Present study	Ref. [64]	Present study
Net power capacity P_{net}, [MW]	393	393	401	401
Turbine parameters:	1150	1150	1150	1150
$T_{t,i}$, [°C]	300	300	300	300
$P_{t,i}$, [bar]	–	0.95	–	0.95
η_t, [−]	640	587	622	586
$\dot{W}_{t,a}$ [MW]				
Compressor parameters:	33	33	33	33
$T_{c,i}$, [°C]	30	30	30	30
$P_{c,i}$, [bar]	0.95	0.95	0.95	0.95
η_c, [−]	134	194	103	198
$\dot{W}_{c,a}$ [MW]				
Combustor parameters:	738	738.30	723	726.8
$T_{co,i}$, [°C]	1264	1189	1200	1154
$\dot{m}_{rCO_2}$ [kg/s]	63	58.4	62	58.33
$\dot{m}_{O_2}$ [kg/s]	15.5	14.6	15.5	14.58
$\dot{m}_{CH_4}$ [kg/s]				
Cycle efficiency, [%]	50.78	48.50	51.8	49.55
Difference in efficiency (%)	4.5		4.3	

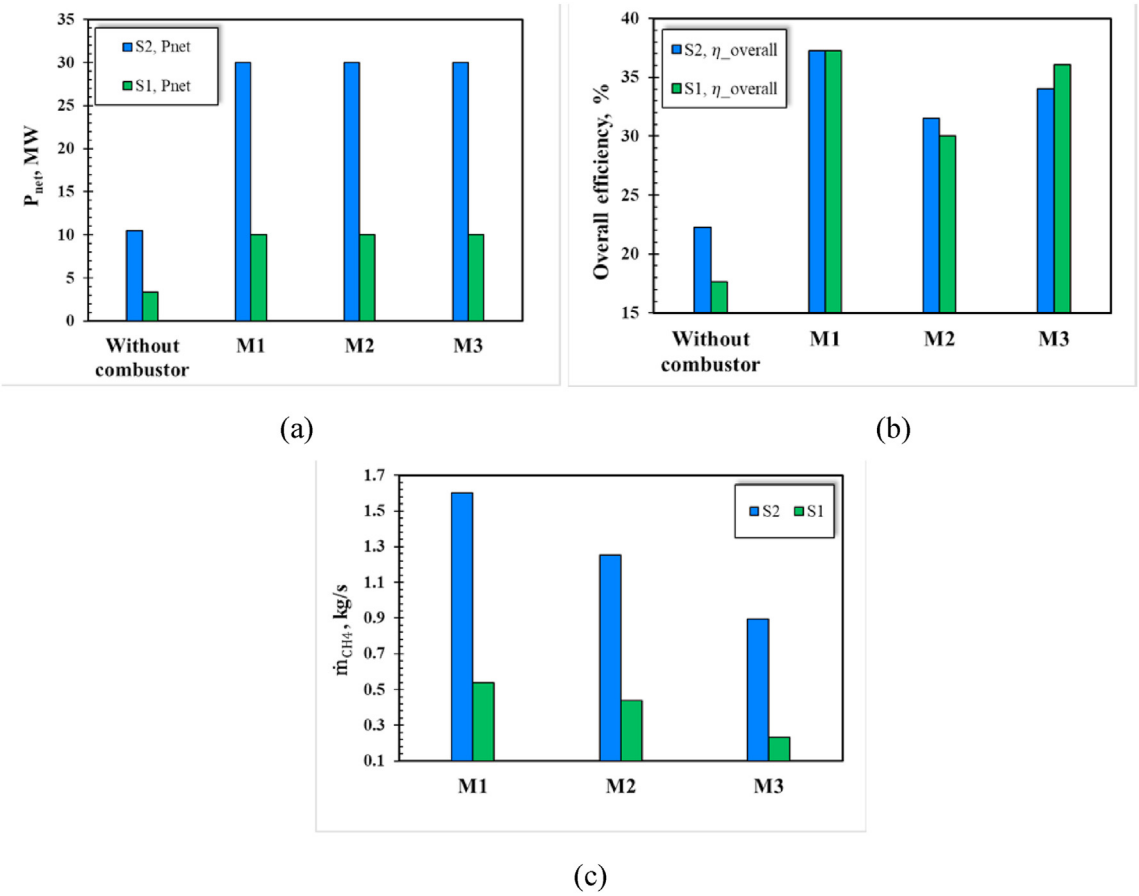

Fig. 7. Effect of combination of the preheater and direct oxy-combustor on a) the net power output, b) overall efficiency, and c) the fuel flow rate of the proposed layouts.

Table 8
Effect of the combination of the preheater and direct oxy-combustor on the performance of the sCO_2 power cycle.

Heat source #	$\dot{W}_{net}$, MW				$\dot{m}_f$, kg/s				$\eta_{overall}$, %			
	Without combustor	M1	M2	M3	Without combustor	M1	M2	M3	Without combustor	M1	M2	M3
S1	3.37	10	10	10	–	0.54	0.44	0.23	17.63	37.26	30.03	36.08
S2	10.50	30	30	30	–	1.60	1.25	0.89	22.23	37.26	31.50	34.05

50 °C by the dry-cooling process. At these conditions, an efficiency of 37.5% is obtained by the present system without-preheater (M1). With preheater, the achieved efficiencies in M2 and M3 are 41.3% and 45.8%, respectively.

The results obtained by the present model are validated by comparison with the data provided by Ricardo [63] and Haseli and Sifat [64] as shown in Table 6. It can be noted that the actual turbine work predicted by the present model is lower and the actual compressor work is higher than the provided data in theses references. This difference is explained by that the compression process in the present study is calculated as a single stage (without multi-inter cooling processes as done in the available literature in Refs. [63,64]). Also, references [63,64] assumed that part of the heat generated by the air separation unit (ASU) is recovered by the recuperator, which enhances the thermal efficiency of the system. In these references, the details of the multi-inter cooling processes and the recovered heat were not provided to facilitate fair and complete comparison with the present study. However, the resulted difference does not exceed 4.5%. No other similar and suitable studies for comparison were found in open literature.

4.2. Preheater and split effects

To explain the effect of the combination of the direct oxy-combustor with the preheater, the performance of the proposed layouts was compared based on four cases as following:

- Case 1: if the power cycle is driven only by the heat source of the preheater (without combustor).
- Case 2: if the power cycle is driven by the combustor without preheater (M1).
- Case 3: if the power cycle is driven by both the combustor and the preheater, which is connected in parallel with the LTR, (M2).
- Case 4: if the power cycle is driven by both the combustor and the preheater, which is connected in parallel with the LTR and the HTR, (M3).

Table 7 shows the details of two heat sources that were utilized for the preheating process. It can be noted that both S1 and S2 have inlet temperatures higher than 550 °C which form a potential source to drive a sCO_2 power cycle. However, the relatively low

Table 9
States, thermal loads and power of the proposed system components.

State	M1				M2				M3			
	T	P	$\dot{m}_{CO_2}$	c_{p,CO_2}	T	P	$\dot{m}_{CO_2}$	c_{p,CO_2}	T	P	$\dot{m}_{CO_2}$	c_{p,CO_2}
	$^\circ C$	bar	kg/s	$\frac{kJ}{kg-^\circ C}$	$^\circ C$	bar	kg/s	$\frac{kJ}{kg-^\circ C}$	$^\circ C$	bar	kg/s	$\frac{kJ}{kg-^\circ C}$
1	750.0	248.35	412.7	1.285	750	249.80	412.7	1.285	750	249.32	412.7	1.285
2	591.5	78.00	412.7	1.216	591.5	78.00	412.7	1.216	591.5	78.00	412.7	1.216
3	301.5	77.56	412.7	1.132	388.6	77.80	412.7	1.155	545.9	77.78	412.7	1.203
4	172.7	75.91	412.7	1.149	270.8	77.64	412.7	1.128	365.8	77.62	412.7	1.148
6	50.0	75.91	406.1	2.36	50.0	77.64	406.7	2.36	50.0	77.62	407.5	2.36
7	149.9	250.00	406.1	1.75	149.9	250.00	406.7	1.75	149.9	250.00	407.5	1.75
8	149.9	250.00	406.1	1.75	149.9	250.00	406.7	1.75	149.9	250.00	407.5	1.75
9	250.4	250.00	406.1	1.343	352.8	249.80	406.7	1.258	486.5	249.84	407.5	1.248
10	250.4	248.35	406.1	1.343	352.8	249.80	406.7	1.258	486.5	249.32	407.5	1.248
11	526.8	248.35	406.1	1.252	548.7	249.80	406.7	1.254	575.8	249.32	407.5	1.258
η_{th} [%]	37.5				41.2				45.8			
$\eta_{overall}$ [%]	37.5				33.9				30.9			
T_{16}	–				400				600			
$Q_{ph}[MW]$	0				55.36				110.52			
$Q_{ltr}[MW]$	59.92				55.36				87.35			
$Q_{htr}[MW]$	140.32				99.31				22.78			
$Q_{oc}[MW]$	119.99				108.53				94.27			
$Q_{cooler}[MW]$	64.15				105.75				174.39			
$\dot{W}_t[MW]$	78.62				78.62				78.62			
$\dot{W}_c[MW]$	25.99				25.99				25.99			
$\dot{m}_{CH_4}\left[\frac{kg}{s}\right]$	2.40				2.17				1.88			
$\dot{m}_{O2}\left[\frac{kg}{s}\right]$	9.60				8.68				7.52			
$\dot{m}_{rCO2}\left[\frac{kg}{s}\right]$	406.10				406.70				407.5			
$\dot{m}_{H2O}\left[\frac{kg}{s}\right]$	5.40				4.85				4.20			
$\dot{m}_{CO2}\left[\frac{kg}{s}\right]$	412.70				412.70				412.7			

mass flow rate of the exhaust gas mixture (EGM) limits the net output power of the cycle if it was driven only by the heat source (Case 1). As shown in Fig. 7 (a), without a combustor, the net output power of the cycle is limited to 3.37 MW for S1 specifications and 10.50 MW for S2 specifications. Furthermore, the overall efficiency of the cycle without combustor was 17.63% and 22.23% for S1 and S2 specifications, respectively (See Table 8 and Fig. 7 (b)). On the other hand, with the presence of the direct oxy-combustor (cases 2 to 4), the net output power can be designed based on the demand and did not limited by the specifications of the heat source of the pre-heater. For instance, the net output power of the last three cases can be three times higher than case 1 (10 MW for S1 specifications and 30 MW for S2 specifications), See Table 8 and Fig. 7 (a). In addition, the overall efficiency of the last three cases was significantly higher than of case 1 as shown in Fig. 7 (b). Based on the reported specifications of S1 and S2 (see Table 7), it can be noted that M1 has the highest overall efficiency followed by M3 and M2 as shown in Fig. 7 (b). This may inform that the insertion of the preheater in M2 and M3 negatively affects the performance of the overall cycle. However, the insertion of the preheater reduces the mass flow rate of the consumed fuel by 22% in M2 and 34% in M3 for S1 and by 28% in M2 and 79% in M3 for S2, see Table 8 and Fig. 7 (c). Moreover, the overall efficiency of M3 is competitive for M1 and higher than M2 by 6% for S1 and 2.5% for S2. This implies that M3 has the potential to be the best economic option as well be discussed in section 4.7.

The insertion of preheater within the direct oxy-fuel sCO_2 cycle affects its performance due to reducing the heating load of the combustor by increasing the inlet temperature of the recycled CO_2 (Table 9, state 11) and due to improving the performance of the recuperators. In the sCO_2 cycle, the specific heat (Cp) of the working fluid is dramatically changing through the components. Inside the recuperators, in conventional cycles (M1), Cp of the cold side (high-pressure) is higher than that of the hot side (low-pressure) with almost equal mass flow rates in both sides. This makes the heat capacity rate (product of the mass flow rate and Cp) of the cold side higher than that of the hot side which results in unbalanced heat transfer process in recuperators. The temperature rise of the cold side will be lower than the temperature decrease of the hot side leading to a "pinch-point" problem. The split flow concept was introduced as a modification for the single flow sCO_2 layouts (including recompression, partial cooling, and preheating layouts) to alleviate the imbalance of Cp near and away from the critical state. This is done by adjusting the mass flow rate of the cold side (adjusting the split ratio) to decrease the heat capacity rate of the cold stream which yields a closed temperature approach and improves the performance of the recuperators.

As mentioned above, S_r is the ratio of the recycled CO_2 that is heated by the LTR (in M2) or by LTR and HTR (in M3) to the total recycled CO_2. For instance, in M2, $S_r = 0.2$ means that only 20% of the recycled CO_2 passes through the LTR, while 80% passes through the preheater. So, the increase of S_r increases the heat capacity rate (HCR) of the cold side (as shown in Fig. 8(a)) relative to the hot side. This yields slight decrease in the cycle efficiency until the HCR of the cold side exceeds that of the hot side. At this point ($S_r = 0.75$), the cycle efficiency sharply decreases up to the value of the conventional system (M1) at $S_r = 1$. Also, on the cold side, the HCR of the LTR is higher than the HTR. This implies that the heat transfer in HTR is more effective than in LTR, which reduces the thermal load of HTR. From Fig. 8(b), the heating contribution of LTR (Q_{ltr}) increases to the maximum point at $Sr = 0.75$ then starts to decrease.

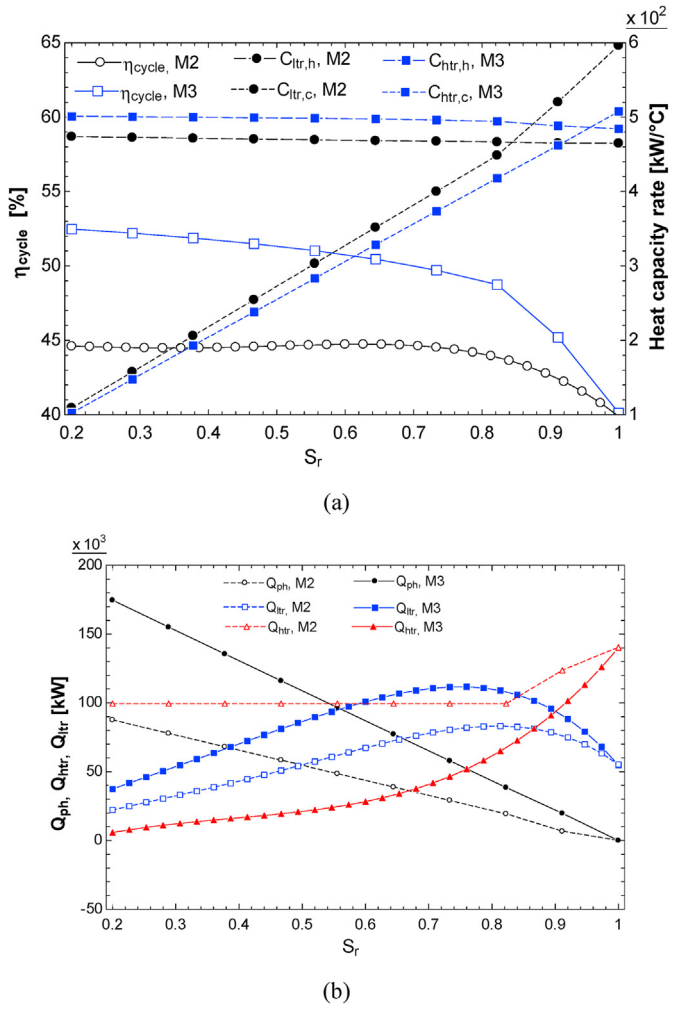

Fig. 8. Variation of (a) overall cycle efficiency (b) thermal loads of heat exchangers with split ratio.

The heating load of HTR (Q_{htr}) in M2 remains constant up to Sr = 0.75 then starts to increase. In M3, the Q_{htr} slowly increases up to S_r = 0.75 then sharply increases to compensate for the reduction of LTR.

The heating process of the recycled CO_2 from the compressor outlet temperature to the TIT is performed by the cycle recuperators and the oxy-combustor in M1. From Fig. 9(a), the HTR provides about 44% of the heating load, the oxy-combustor provides 37%, while the LTR provides 19%. After the implementation of the split flow, the contribution of the HTR is reduced to 31% while the preheater contribution is very close to the contribution of the LTR (in M2) since the split ratio is fixed at 0.5. However, the contribution of the LTR increased to 28% while decreased to 7% for the HTR in M3. Also, the combustor contribution reduces to 30% in M3. That means the split flow in M3 enhances the heat recovery through the LTR which minimizes the contribution of the HTR. The HTR is incorporated within the cycle to reduce the irreversibility and to enhance the heat recovery. So, it can be concluded that the preheating process along with the split flow in M3 scenario reduces the overall size of the recuperators and increases cycle efficiency. Furthermore, the preheater creates an opportunity to utilize moderate-temperature waste heat sources.

While the preheater improves the cycle efficiency and enhances the outlet temperatures from recuperators in the cold side, it affects the recuperators outlet temperature in the hot side. As the split ratio is reduced, the preheater load is increased and so the precooler load. For instance, at the design point, the cooler inlet temperature (T4) in M3 is higher than that of M2 and in M2 is higher than M1. Thus, the size of the cooler is increased with the increase of T4. So, to improve the cycle efficiency and the performance of the recuperators with a feasible cooler size, the split ratio should be optimized. For the selected design point of this work, the optimum split ratio is found at Sr = 0.75 (Fig. 8). At this ratio, the thermal loads of the preheater, cooler, and HTR are much lower than that of LTR with a thermal efficiency of 41.7% in M2 and 45.8% in M3.

4.3. *Effect of high and low pressures*

Fig. 10(a) shows the variation of the cycle efficiency of each

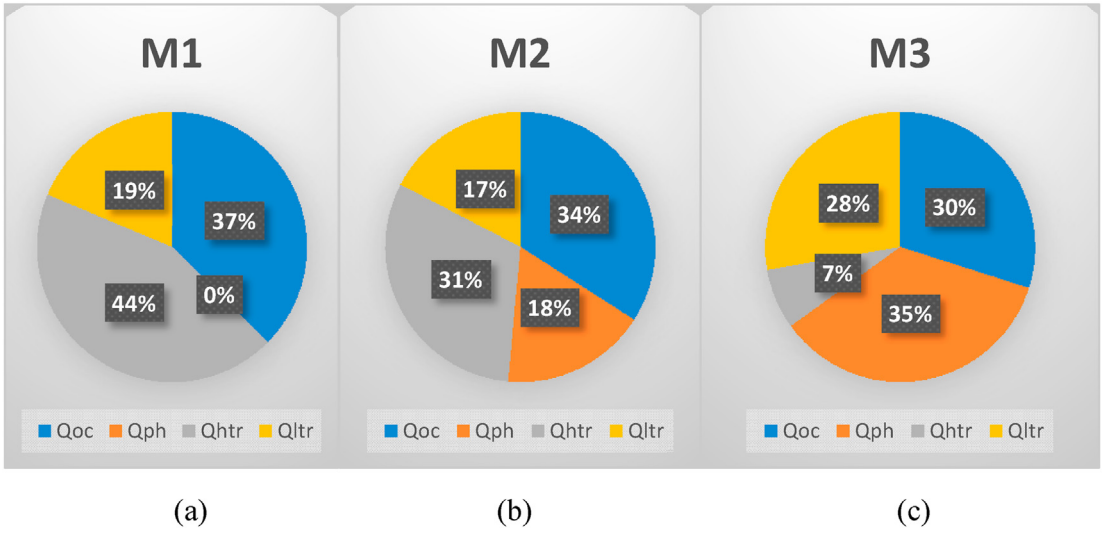

Fig. 9. Thermal contribution of the oxy-combustor, HTR, LTR, and preheater at design point.

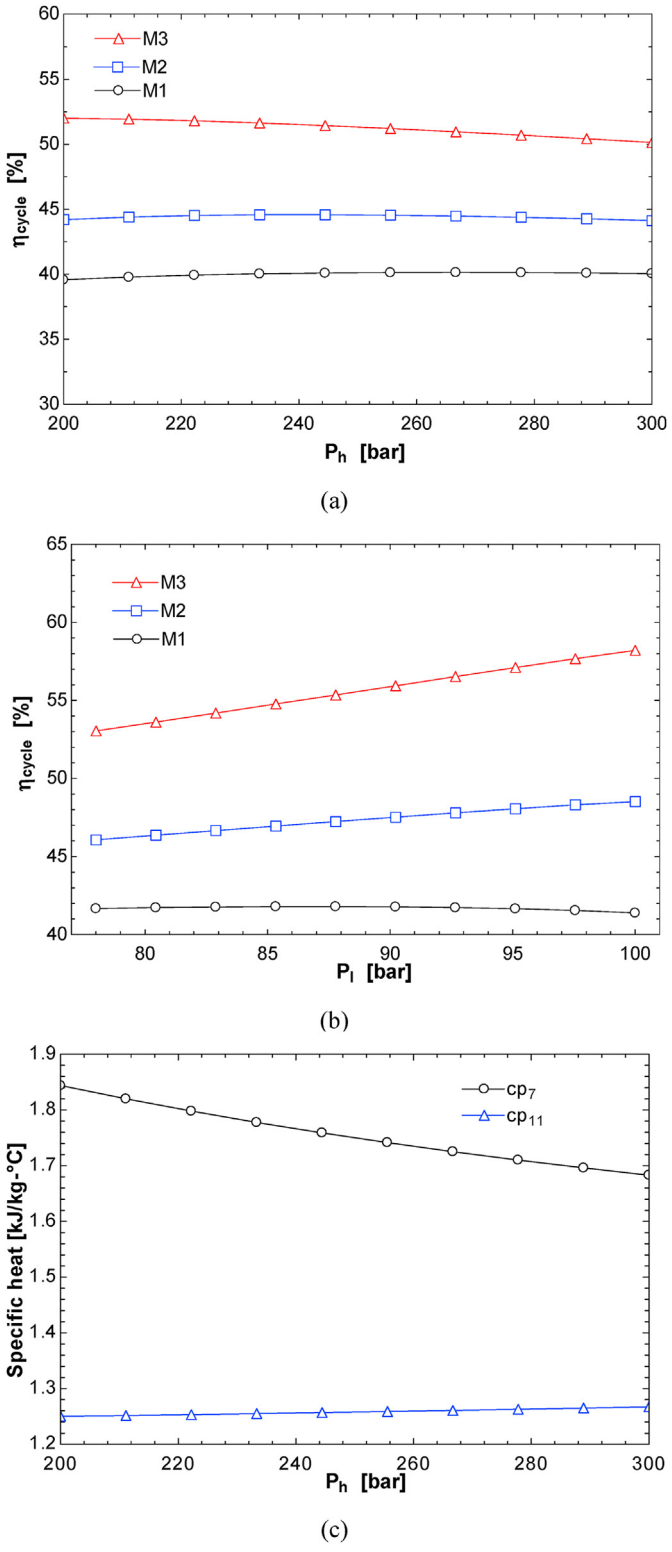

Fig. 10. Variation of cycle efficiency with (a) high-pressure, (b) low-pressure. (c) Variation of specific heat with high-pressure at compressor outlet (cp_7) and combustor inlet (cp_{11}).

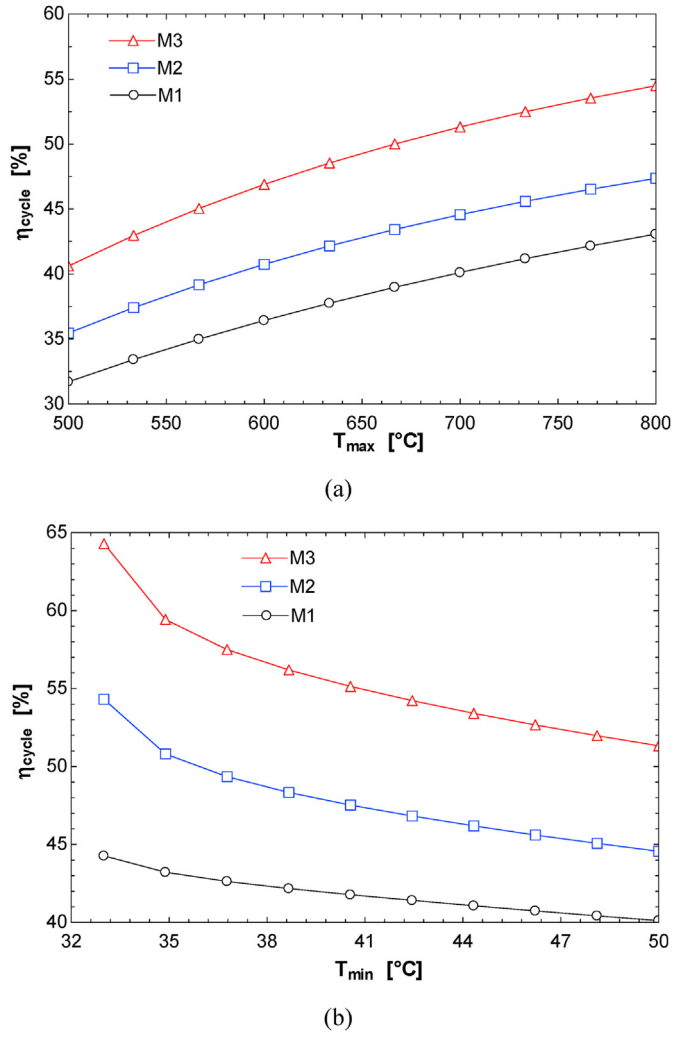

Fig. 11. Variation of cycle efficiency with (a) maximum temperature and (b) minimum temperature.

mode with the increase of the high-pressure while the other input parameters are kept fixed at the design values (see Table 2). It can be noted that as the turbine inlet pressure (the high pressure) increases, the cycle efficiency remains almost the same in M1 and M2, while tends to decrease in M3. However, the cycle efficiency of M3 is higher than that of M2 by 3.74% and of M1 by 8.21% for P_h range of 200–300 bar.

In contrast to the high-pressure effect, the increase of the lower pressure (Fig. 10(b)) increases the cycle efficiency in M3 and M2 while tends to remain the same in M1. For M1, when P_h is increased with fixed P_l, the pressure ratio PR=P_h/P_l increases, the thermal efficiency is increased. While when P_l increases with fixed P_h, the PR decreases, the thermal efficiency is decreased. For M2, the addition of pre-heater, resulted in reducing Q_{oc} causing the efficiency to go up by 3.74% compared to M1. In M3 the efficiency went up by 8.3% compared to M1 because Q_{oc} is reduced much more compared to M2. This means that M3 is more effective in contributing heat to reduce Q_{oc}. The decrease in efficiency in M3 as P_h increases with fixed P_l is explained by the decrease of Cp of the sCO2 at compressor outlet with higher pressure as shown in Fig. 10(c). This, in turn, reduces the effect of the recovered heat by recuperators which results in lower temperatures at the combustor inlet, which requires more heat by the combustor to reach the design TIT. However, this reduces the cycle efficiency only by 1.30%.

Table 10
Range of available temperature in some waste heat sources [67].

Type of device	Temperature (°C)
Annealing furnace cooling systems	425–650
Catalytic crackers	425–650
Heat treating furnaces	425–650
Reciprocating engine exhausts	315–595
Drying and baking ovens	230–595
Gas turbine exhausts	370–540
Steam boiler exhausts	230–480

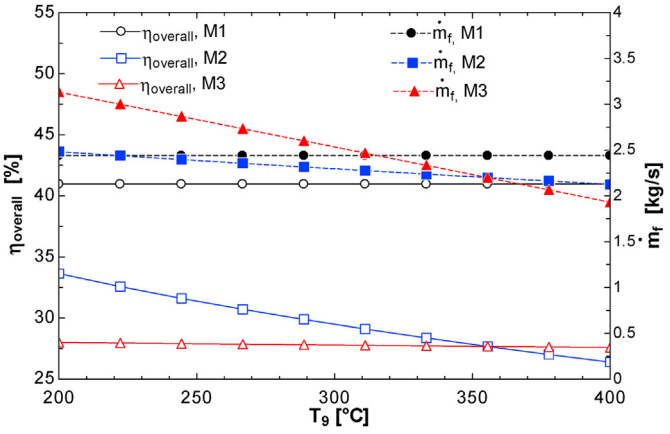

Fig. 12. Effect of preheater outlet temperature on overall efficincy and fuel mass flow rate.

4.4. Effect of maximum and minimum temperatures

Higher TIT (T_{max}) yields higher thermal efficiency as shown in Fig. 11(a). Usually, the TIT is limited by the thermal properties of the turbine materials. However, the sCO_2 cycle achieves high efficiencies with moderate TITs. So, in Fig. 11(a), the TIT is set to be within the range of 500–800 °C with T_{min} kept fixed at 50 °C. In this range, the cycle efficiency is improved by 7.88% in M3 and by 3.70% in M2 compared to M1. The main drawback of increasing T_{max} is that it increases the required sizes of all heat exchangers. While the increase of T_{max} improves the cycle efficiency, the opposite is true for the increase of T_{min} as shown in Fig. 11(b) (with $T_{max} = 750$ °C). As the inlet compressor temperature (T_{min}) is close to the critical temperature of the CO_2, the cycle efficiency jumps to 52.48% in M3, 46.79% in M2, and 40.31% in M1. However, for dry cooling conditions, the design value of T_{min} is set to 50 °C. This value is achievable by dry cooling process, where the lower pressure can be adjusted to the optimum value. Furthermore, in the case of dry cooling, the intercooling compression can enhance the cycle efficiency. However, to focus on the effects of the preheater, the other possible improvements (such as reheating, dual expansion, precompression, and intercooling compression) are not investigated in this study.

4.5. Overall performance with preheating process

In this section, the effect of the heating load provided by the preheater on the overall performance of the cycle is discussed. As shown in Table 10, there are several waste-heat resources with available temperature in the range of 200–500 °C in which, the recovery of waste heat by the preheater of the sCO2 cycle reduces the amount of combusted fuel as shown in Fig. 12. However, the overall efficiency of the cycle is reduced due to the heat added to the preheater. It is found that the overall efficiency of the cycle

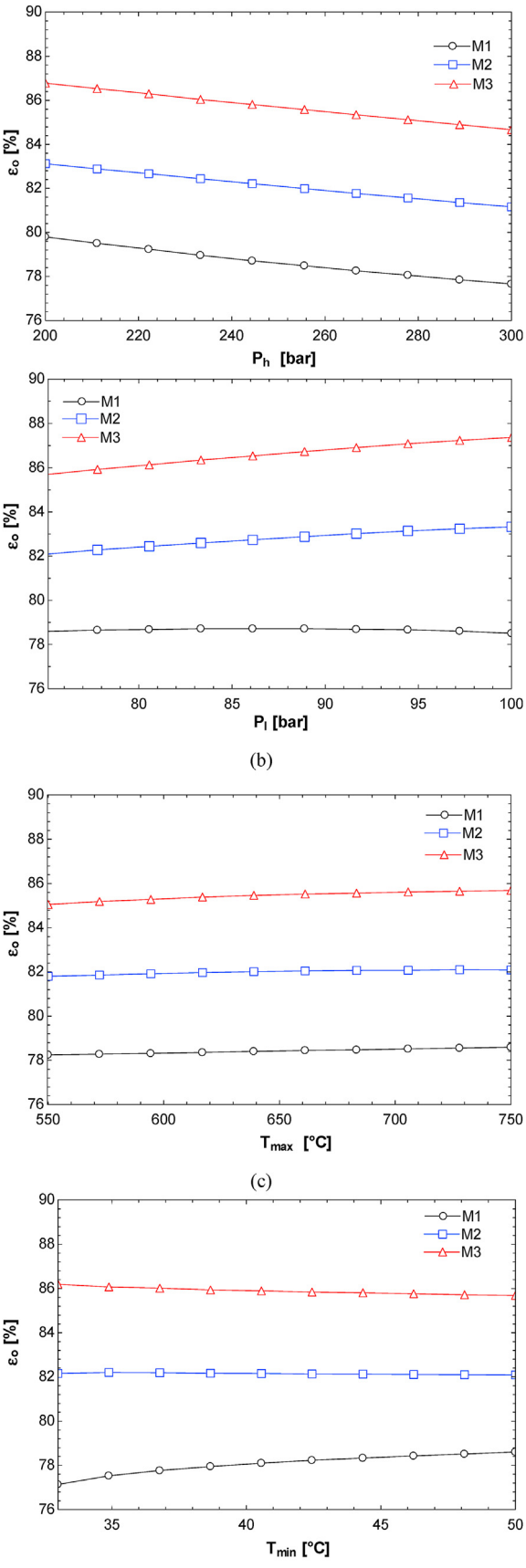

Fig. 13. Variation of the overall second law efficiency with a) high pressure, b) low pressure, c) maximum temperature, and d) minimum temperature.

Table 11
Second-law efficiency of cycle components in M1, M2, and M3 at $P_h = 250$ bar, $P_l = 75$ bar, $T_{max} = 750$ °C, and $T_{min} = 50$ °C.

Configuration	Combustor	Turbine	Compressor	Recuperators	Preheater	Precooler	Overall cycle
	%	%	%	%	%	%	%
M1	75.56	98.92	89.50	68.21	–	86.88	84.22
M2	78.04	98.92	89.50	77.72	73.27	82.52	86.52
M3	81.20	98.92	89.50	90.86	88.68	77.95	88.78

without-preheater (M1) at the design point conditions (except $P_l = 78$ bar) is 41% with a fuel mass flow rate of 2.5 kg/s. The outlet temperature of the working fluid passing through the preheater (T9 in M2 and M3) depends on the available temperature of the waste heat sources. It is found that the overall efficiency of the cycle decreases with the increase of T9 alongside with a decrease in the required flow rate of the fuel. If T9 is designed to be in the range of 200−400 °C, as shown in Fig. 12, the overall efficiency of the cycle decreases from 34% to 27% in M2 and stabilizes at 28% in M3. Comparing the mass flow rate of the fuel, it is found that the fuel flow rate reduces from 2.5 to 2.1 kg/s in M2. In M3, it reduces from 3.2 to 1.8 kg/s which means that the operation of M3 consumes more fuel than in M2 at outlet temperature less than 360 °C. This means that M3 is suitable for waste heat resources with high temperature (360 °C) and M2 is more suitable for waste heat with lower temperatures.

4.6. Exergy analysis results

In this section, the second law efficiency of the three layout configurations is analyzed for the overall cycle as well as for each component. The effects of the major operating conditions on the overall second law (exergy) efficiency (ε_o) are presented in Fig. 13. Based on the design range of these conditions, it can be noted that ε_o of M3 is the highest and of M1 is the lowest. This is explained by that the splitting-preheating process reduces the mass flow rates as well as the temperature differences across the combustor, recuperators, and the precooler (major sources of the irreversibility).

As shown in Fig. 13(a), the increase of the high pressure reduces ε_o of the cycle. This returns to that higher-pressure that yields higher temperatures at the exit of the compressor, which in turn reduces the recuperative heat by the recycled sCO_2 and increases the temperature at the inlet of the precooler. Furthermore, this reduces the temperature at the inlet of the combustor. Aa a result, the temperature differences across the compressor, recuperators, combustor, preheater, and precooler are increased and their ε_o are decreased at higher cycle pressures. The increase of the higher pressure from 200 to 300 bar reduces ε_o of M1 from 79.80% to 77.66% ($\Delta\varepsilon_o = 2.14\%$), of M2 from 83.12% to 81.16% ($\Delta\varepsilon_o = 1.96\%$), and of M3 from 86.78% to 84.67% ($\Delta\varepsilon_o = 2.11\%$), implying that the sensitivity of ε_o for the higher pressure is reduced with the splitting-preheating process applied in M2 and M3.

In contrast to the higher pressure, the increase of the lower pressure improves the ε_o of the three layout configurations as shown in Fig. 13(b). It is noted that the increase of the lower pressure (from 75 to 100 bar) slightly reduces the exergy efficiency of the compressor (by 1.39%). The increase of the lower pressure reduces both the fuel and product exergies of the compressor. However, the reduction of the product exergy is larger than of the fuel exergy which results in less compressor ε_o. Furthermore, the increase of the lower pressure reduces the temperature at the outlet of the compressor which enhances the performance of the recuperators and yields a higher temperature at the inlet of the combustor. Also, higher pressure at the turbine outlet means higher temperatures too. So, the temperature differences increase across the recuperators and reduce across the combustor, turbine, and the precooler. This implies that ε_o of the later components are improved (by 4.06%, 1.08%, and 3.62%, respectively) with the increase of the lower pressure which yields a higher overall exergy efficiency.

Table 12
Temperatures at the inlets and outlets of the three layout components at $P_h = 250$ bar, $P_l = 75$ bar, $T_{max} = 750$ °C, and $T_{min} = 50$ °C.

Configuration	T_1,°C	T_{2a},°C	T_4,°C	T_6,°C	T_{7a},°C	T_{11},°C
M1	750	586	178	50	156	525
M2	750	586	216	50	156	545
M3	750	586	255	50	156	565

The increase of TIT reduces the ε_o of the precooler by 1.03% over its range while ε_o of the combustor and recuperators are improved by 5.03%, 2.55%, respectively. This yields to higher overall ε_o with higher TIT as shown in Fig. 13(c). While the increase of CIT reduces the energy efficiency of the cycle, it increases the exergy efficiency in M1 and reduces it in M2 and M3 as shown in Fig. 13(d) by less than 1% in all configurations. The behavior of M1 curve results from the increase of the recycled sCO2 temperature at the inlet of the combustor which improves its ε_o higher than the slight reduction occurs in ε_o of the precooler.

Table 11 shows ε_o of the components of each layout at the design point conditions ($T_{max} = 750$ °C, $T_{min} = 50$ °C, $P_h = 250$ bar, $P_l = 5$ bar, and $P_{net} = 50$ MW) and optimum Sr = 0.75. It can be noted that $\varepsilon_o$of the compressor and turbine remain constant in the three layout configurations. Also, ε_o of the recuperators and the combustor are increased while of the precooler is decreased. The reduction of the precooler ε_o (from 86.88% in M1 to 77.95% in M3) returns to that its inlet temperature in M2 and M3 is higher than in M1 (see T_4 in Table 12) which increases both the exergy destruction and exergy losses across its wall to the environment (cooling fluid). In contrast, the temperature at the inlet of the combustor in M2 and M3 is higher than in M1 which improves its ε_o (from 75.56% in M1 to 81.20% in M3). Regarding the recuperators, the temperature differences in the hot side ($T_{2a}-T_4$) are 408 °C for M1, 370 °C for M2, and 331 °C for M3 while in the cold side ($T_{11}-T_{7a}$) are 369 °C for M1, 389 °C for M2, and 409 °C for M3. This means that the amount of the temperature difference reduction in the hot side is larger than the increase in the cold side. Furthermore, the splitting of the recycled sCO2 in M2 and M3 minimizes the pressure losses across LTR, HTR, and preheater. All of these notes explain the reasons for the increase in $\varepsilon_o$of the recuperators from 68.23% in M1 to 90.86% in M3.

Fig. 14 presents the exergy destruction portion of each component from the total exergy destruction in each configuration at the design point conditions. Compared to exergy share in M1, it can be noted that the percentage of the HTR reduces by 14% in M2 and by 15% in M3. In contrast, the exergy destruction of the precooler

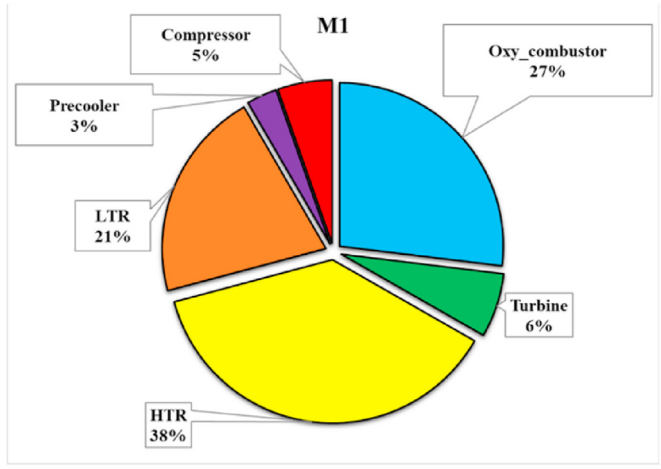

(a)

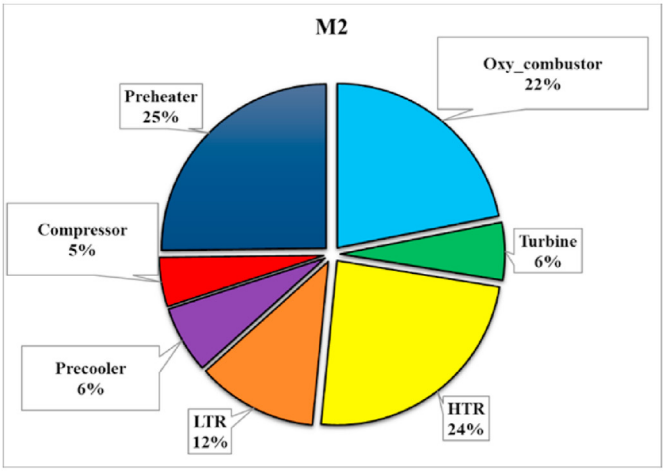

(b)

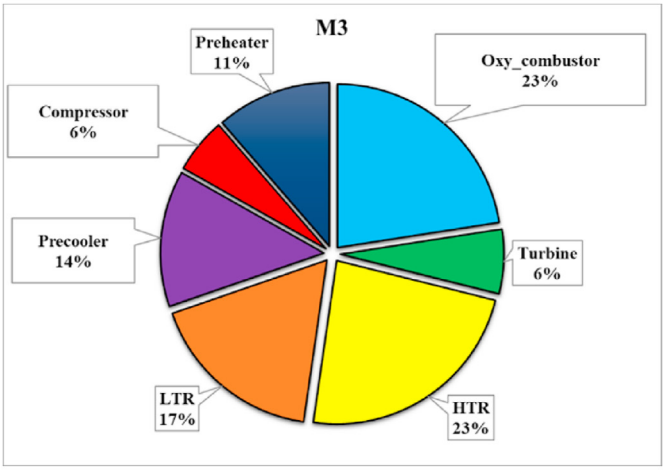

(c)

Fig. 14. Exergy destruction of each layout component in a) M1, b) M2, and c) M3 at $P_h = 250$ bar, $P_l = 75$ bar, $T_{max} = 750$ °C, and $T_{min} = 50$ °C.

increases by 3% in M2 and by 11% in M3. Furthermore, the portion of the LTR is minimum in M2 and maximum in M3. Similarly, the preheater portion reduces from 25% in M2 to 11% in M3. This explained by that the temperature difference between the inlet of the heat source stream (T_{16}) and the temperature of the recycled CO_2 at the exit of the preheater (T_9) is much lower than in M2 which improves the exergy efficiency of the preheater and minimizes its contribution to the total exergy destruction. This confirms that the preheating process improves the exergetic performance of the recuperators and oxy-combustor which improves both energetic and exergetic efficiencies. However, the size and performance of the precooler are negatively affected by these modifications. So, it is necessary to investigate the three layout configurations based on an exergoeconomic approach to evaluate the effectivity of adding the preheating process within the basic layout (M1).

4.7. Exergoeconomic analysis results

Fig. 15 simulates the variation of the total product unit cost ($c_{p,total}$) of each configuration with the variation of a) the maximum temperature and b) the PR of the cycle. Fig. 15 (a) shows that the

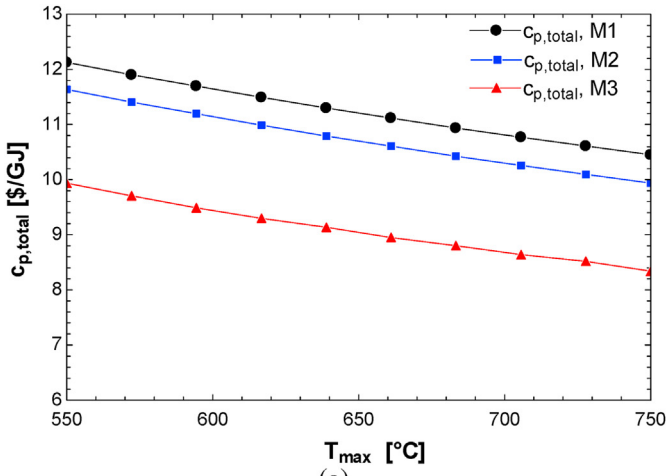

(a)

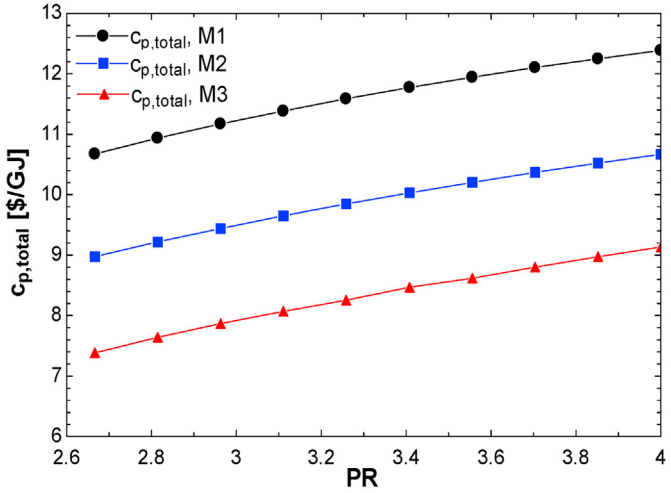

(b)

Fig. 15. Variation of total product unit cost and overall exergetic efficiency with a) maximum temperature, b) PR.

Table 13
Exergoeconomic analysis at $P_h = 250$ bar, $P_l = 75$ bar, $T_{max} = 750$ °C, and $T_{min} = 50$ °C.

Components	M1				M2				M3			
	$\dot{E}_{D,k}$,(MW)	$\dot{C}_{D,k}$,($/h)	$\dot{Z}_k$,($/h)	f_k,(%)	$\dot{E}_{D,k}$,(MW)	$\dot{C}_{D,k}$,($/h)	$\dot{Z}_k$,($/h)	f_k,(%)	$\dot{E}_{D,k}$,(MW)	$\dot{C}_{D,k}$,($/h)	$\dot{Z}_k$,($/h)	f_k,(%)
Oxy-combustor	22.1	1352.0	976.6	41.95	19.4	1051.0	830	44.1	17.1	900.6	749.3	45.4
Turbine	5.2	234.5	191.2	44.9	5.0	226.3	191.1	45.8	4.8	217.6	191.0	46.7
Compressor	4.4	88.1	34.3	28.0	4.3	85.6	34.5	28.7	4.1	82.6	34.5	29.5
HTR	30.9	323.3	14.5	4.3	21.3	547.5	14.8	2.6	10.3	711.5	15.0	2.1
LTR	17.1	238.7	9.0	3.6	10.5	360.1	9.0	2.4	13.2	468.1	9.0	1.9
Preheater	–	–	–	–	2.4	90.2	2.4	0.7	3.8	35.2	4.7	17.2
Precooler	2.5	163.2	11.1	6.4	5.9	479.2	11.4	2.3	10.2	601.1	11.8	1.9
Energetic-efficiency(%)	37.5				41.3				45.8			
Exergetic-efficiency(%)	78.1				86.5				88.8			
Total product unit cost($/GJ)	11.68				9.94				8.34			

total product unit cost (TPUC) decreases with the increase of the turbine inlet temperature (T_{max}). The increase of T_{max} from 550 to 750 °C reduces the TPUC by 1.48$/GJ in M1, 1.70$/GJ in M2, and 1.63$/MJ in M3. However, the TPUC of M1 is higher than of M2 and M3. The $c_{p,total}$ is reduced by 34.96% in M3 and by 13.92% in M2 compared to its values in M1. Fig. 15 (b) represents the variation of the TPUC with the increase of PR ($PR=P_h/P_l$). The lower pressure is fixed at 75 bar while the higher pressure is changed from 200 to 300 bar. Also, in Fig. 15 (b), T_{max} is fixed at 750 °C. The increase of PR from 2.6 to 4 increases the TPUC by 1.72$/GJ in M1, 1.83$/GJ in M2, and 1.74$/GJ in M3. Furthermore, similar to Fig. 15(a), the TPUC is reduced by 34.66% in M3 and by 14.27% in M2 compared to M1. Table 13 compares the exergoeconomic results of the three layout configurations at the design point conditions. It is noted that the exergoeconomic factor (f_k) of the oxy-combustor, turbine, and compressor are maximum in M3 and minimum in M1. However, f_k of recuperators and precooler is negatively affected due to the increase of the exergy destruction cost $\dot{C}_{D,k}$. Furthermore, it can be noted that f_k of the recuperators, preheater, and precooler is much lower than f_k of the other components in all layout configurations. This is returned to two reasons: 1) the capital cost of the heat exchanger components (HTR, LTR, preheater, and precooler) is lower than turbomachinery components (turbine and compressor) and 2) the exergy destruction cost $\dot{C}_{D,k}$ of the heat exchanger components is higher than of the turbomachinery components.

As shown in the last three rows of Table 13, the energetic efficiency increases by 3.8% in M2 and 8.3% in M3 compared to M1 (37.5%). Also, the exergetic efficiency increases by 8.4% in M2 and 10.7% in M3 compared to its value in M1 (78.1%). Furthermore, the TPUC decreases by 1.74 $/GJ in M2 and 3.34$/GJ in M3 compared to its value in M1 (11.68$/GJ). This emphasizes the effectiveness of adding a preheater in parallel with the LTR (M2) which is achievable when integrated with a waste heat source at medium temperatures (200–400 °C). Also, adding a preheater in parallel with the LTR and HTR is effective with a waste heat source at temperatures above 400 °C as those used in section 4.2.

4.8. Economic assessment of the proposed configurations

The economic evaluation of the proposed configurations is performed in terms of the levelized cost of electricity (LCOE) which is calculated according to Eq. (49) [68].

$$LCOE = \frac{PC - PV_{DTS} + PV_{LOC} - PV_{SC}}{LEP} \quad (49)$$

where PC is the project cost, which is the sum of the components' and installation costs (given in Eq. (50)), PV_{DTS} is the present value of the depreciation tax shield (given in Eq. (51)), PV_{LOC} is the present value of lifetime operating costs (given in Eq. (52)), PV_{SC} is the present value of salvage costs (assumed $0.00), and LEP is the lifetime electrical production (given in Eq. (53)).

$$PC = \sum (Component\ cost + Installation\ cost)_k \quad (50)$$

$$PV_{DTS} = TR \times PC \Big/ (1 + DR)^{DP} \quad (51)$$

$$PV_{LOC} = n^*(OMC + Cost\ of\ the\ fuel + Waste\ heat\ cost) \Big/ (1 + DR)^n \quad (52)$$

$$LEP = PUF \times n \times \dot{W}_{net} \times 8760 \quad (53)$$

The installation costs were taken as 12% of the components'

Table 14
Input parameters of the LCOE model.

Parameter	Value
Plant lifetime (years)	20
Depreciation period (DP) (years)	10
Tax rate (%)	35
Plant utilization factor (PUF) (%)	85
Cost of the fuel ($/kWh)	0.07
Operating and maintenance cost ($/kWh)	0.008
Discount rate (%)	2

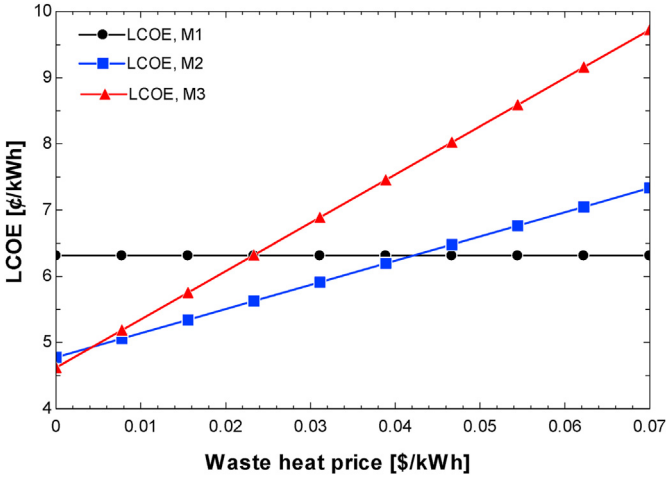

Fig. 16. Effect of the waste heat price on the LCOE of the proposed configurations at $P_h = 250$ bar, $P_l = 75$ bar, $T_{max} = 750$ °C, $T_{min} = 50$ °C, and $T_{16} = 554$ (for M2) and (680) for (M3).

Table 15
Comparison between the recuperators of the proposed configurations in terms of their loads and heat transfer areas at $P_h = 250$ bar, $P_l = 75$ bar, $T_{max} = 750\,^{\circ}C$, $T_{min} = 50\,^{\circ}C$, and $T_{16} = 554$ (for M2) and (680) for (M3).

Parameter	M1	M2	M3
Heat transferred by the HTR Q_{HTR} (kW)	149,207	106,582	48,944
Heat transferred by the LTR Q_{LTR} (kW)	65,193	86,383	122,044
Heat transferred by the preheater Q_{ph} (kW)	0	27,157	54,199
Heat transferred by the precooler Q_{pc} (kW)	72,056	91,726	112,107
Heat transfer area of the HTR A_{HTR} (m^2)	10,725	11,150	5760
Heat transfer area of the LTR A_{LTR} (m^2)	4751	4472	4011
Heat transfer area of the preheater A_{PH} (m^2)	0	560.4	2356
Heat transfer area of the precooler A_{pc} (m^2)	7400	7820	8201
Total cost of the HTR, LTR, preheater, and precooler (Million $)	8.01	8.57	7.91

costs, which are presented in Table 4. The other parameters of the LCOE model are presented in Table 14.

To illustrate the effect of the waste heat price (WHP) on the LCOE; , compared to being available free, of each configuration, a range of WHP from 0 to 7¢/kWh is studied and the results are shown in Fig. 16. For free waste heat (WHP = 0), the LCOE is 6.353¢/kWh for M1, 5.505¢/kWh for M2, and 4.719¢/kWh for M3. It is clear that M3 has the lowest LCOE as a result of the reduction of the consumed fuel and the reduction of the total cost of the heat exchangers (LTR, HTR, preheater, and precooler) as shown in Table 15. However, as the WHP increases, the economic benefits of M2 and M3 over M1 are diminishing. At WHP higher than 2.4¢/kWh, the LCOE of M1 becomes less than of M3 and at WHP higher than 4.2¢/kWh, the LCOE of M1 becomes less than of both M2 and M3. Furthermore, it can be noted that the LCOE of M3 is less than M2 only for WHP less than 0.8¢/kWh. This returns to the fact that the heat provided by the preheater in M3 is much larger than in M2 (see Table 15) which significantly increases the LCOE of M3 over M2 at high prices of the waste heat. Moreover, as discussed in section 4.2, the performance of the LTR in M3 recovers more heat with lower heat transfer area than in M1 and M2. To summarize, M3 cycle configuration provides enhanced cycle efficiency by minimizing fuel consumption and requires less bulky (more compact) recuperators than the other configurations, however M3 requires waste heat source with higher temperatures and flow rate than in M2. Economically, M3 still the best configuration at WHP less than 0.8¢/kWh.

5. Conclusions

Novel direct-fired oxy-fuel combustion sCO_2 power cycle with-preheater is investigated and optimized using energetic, exergetic, and exergoeconomic analyses. The preheater is integrated within the original layout of the sCO_2 cycle (M1) in two additional layouts; in parallel with low-temperature recuperator (M2) and with both reciprocators (M3). Novelty aspects of the study include investigation of preheater effect on the performance of the sCO_2 cycle at moderate turbine inlet temperatures and dry-cooling conditions. Results show that the overall efficiency is improved by 3.7% in M2 and by 8.3% in M3 compared to M1. Furthermore, the split flow at the compressor downstream enhances the performance of the recuperators by reducing the “pinch-point” effect. However, the split flow increases the temperature at the inlet of the cooler, which means larger size and capacity cooler is required. To obtain a reasonable size for both the precooler and the preheater, the split ratio was optimized based on selected design conditions. The optimum split ratio is 0.75 with overall efficiency of 45.8% in M3, 41.2% in M2, and 37.5% in M1 for 50MW_e system at turbine inlet temperature of 750 °C, compressor inlet temperature of 50 °C, high pressure of 250 bar and low pressure of 75 bar. The exergy efficiency of the cycle is increased from 78.1% in M1 to 86.5% in M2 and 88.8% in M3. The exergoeconomic analysis in the present study is the first to be applied to direct-fired oxy-fuel sCO_2 cycle. Results of the exergoeconomic analysis show that the total product cost per unit exergy reduces from 11.68$/GJ in M1 to 9.94$/GJ in M2 and 8.34$/GJ in M3.

Credit author statement

Ahmad K. Sleiti: Conceptualization, Methodology, Investigation, Writing-Original Draft, Review & Editing, Formal analysis, Resources, Funding acquisition, Project administration, Supervision, Visualization. **Wahib Al-Ammari**: Investigation, Data Curation, Writing-Original Draft, Software, Validation, Editing. **Samer F. Ahmed:** Conceptualization, Review & Editing, Visualization. **Jayanta S. Kapat:** Conceptualization, Visualization, Review & Editing.

Declaration of competing interest

The authors declare that they have no known competing financial interests or personal relationships that could have appeared to influence the work reported in this paper.

Acknowledgments

The work presented in this publication was made possible by NPRP-S grant # [11S-1231–170155] from the Qatar National Research Fund (a member of Qatar Foundation). The findings herein reflect the work, and are solely the responsibility, of the authors.

References

[1] Li MJ, Zhu HH, Guo JQ, Wang K, Tao WQ. The development technology and applications of supercritical CO2 power cycle in nuclear energy, solar energy and other energy industries. Appl Therm Eng 2017;126:255–75. https://doi.org/10.1016/j.applthermaleng.2017.07.173.
[2] Elbeih MB, Sleiti AK. Analysis and optimization of concentrated solar power plant for application in arid climate. Energy Sci Eng 2021;2021(00):1–14. https://doi.org/10.1002/ese3.742.
[3] Sleiti AK, Al-ammari WA, Al-khawaja M. A novel solar integrated distillation and cooling system – design and analysis. Sol Energy 2020;206:68–83. https://doi.org/10.1016/j.solener.2020.05.107.
[4] Naimaster EJ, Sleiti AK. Potential of SOFC CHP systems for energy-efficient commercial buildings. Energy Build 2013;61. https://doi.org/10.1016/j.enbuild.2012.09.045.
[5] Sleiti AK. Tidal power technology review with potential applications in Gulf Stream. Renew Sustain Energy Rev 2017. https://doi.org/10.1016/j.rser.2016.11.150.
[6] Zhu Z, Chen Y, Wu J, Zhang S, Zheng S. A modified Allam cycle without compressors realizing efficient power generation with peak load shifting and CO2 capture. Energy 2019. https://doi.org/10.1016/j.energy.2019.01.165.
[7] Olumayegun O, Wang M, Oko E. Thermodynamic performance evaluation of supercritical CO2 closed Brayton cycles for coal-fired power generation with solvent-based CO2 capture. Energy 2019;166:1074–88. https://doi.org/10.1016/j.energy.2018.10.127.
[8] Luo D, Huang D. Thermodynamic and exergoeconomic investigation of various

SCO2 Brayton cycles for next generation nuclear reactors. Energy Convers Manag 2020;209:112649. https://doi.org/10.1016/j.enconman.2020.112649.
[9] Ahn Y, Bae SJ, Kim M, Cho SK, Baik S, Lee JI, et al. Review of supercritical CO2 power cycle technology and current status of research and development. Nucl Eng Technol 2015;47:647–61. https://doi.org/10.1016/j.net.2015.06.009.
[10] Liao G, Liu LEJ, Zhang F, Chen J, Deng Y, et al. Effects of technical progress on performance and application of supercritical carbon dioxide power cycle: a review. Energy Convers Manag 2019;199:111986. https://doi.org/10.1016/j.enconman.2019.111986.
[11] Crespi F, Sánchez D, Rodríguez JM, Gavagnin G. Fundamental thermo-economic approach to selecting sCO2 power cycles for CSP applications. Energy Procedia; 2017. p. 963–70. https://doi.org/10.1016/j.egypro.2017.09.215.
[12] Angelino G. Carbon dioxide condensation cycles for power production. J Eng Gas Turbines Power 1968;90:287–95. https://doi.org/10.1115/1.3609190.
[13] Feher EG. The supercritical thermodynamic power cycle. Energy Convers 1968;8:85–90. https://doi.org/10.1016/0013-7480(68)90105-8.
[14] Dostal V, Driscoll MJ, Hejzlar P. A supercritical carbon dioxide cycle for next generation nuclear reactors. 2004. https://doi.org/MIT-ANP-TR-100.
[15] Binotti M, Astolfi M, Campanari S, Manzolini G, Silva P. Preliminary assessment of sCO2 cycles for power generation in CSP solar tower plants. Appl Energy 2017;204:1007–17. https://doi.org/10.1016/j.apenergy.2017.05.121.
[16] Luu MT, Milani D, McNaughton R, Abbas A. Analysis for flexible operation of supercritical CO2 Brayton cycle integrated with solar thermal systems. Energy 2017;124:752–71. https://doi.org/10.1016/j.energy.2017.02.040.
[17] Al-Sulaiman FA, Atif M. Performance comparison of different supercritical carbon dioxide Brayton cycles integrated with a solar power tower. Energy 2015;82:61–71. https://doi.org/10.1016/j.energy.2014.12.070.
[18] Mehrpooya M, Sharifzadeh MMM. A novel integration of oxy-fuel cycle, high temperature solar cycle and LNG cold recovery – energy and exergy analysis. Appl Therm Eng 2017;114:1090–104. https://doi.org/10.1016/j.applthermaleng.2016.11.163.
[19] Yang J, Yang Z, Duan Y. Off-design performance of a supercritical CO2 Brayton cycle integrated with a solar power tower system. Energy 2020;201:117676. https://doi.org/10.1016/j.energy.2020.117676.
[20] Qiao Z, Tang Y, Zhang L, Pan C, Romero CE, Wang X, et al. Design and performance analysis of a supercritical CO2 (sCO2)-water separator for power generation systems using hot sCO2 from geothermal reservoirs. Geothermics 2019;81:123–32. https://doi.org/10.1016/j.geothermics.2019.05.001.
[21] Qiao Z, Cao Y, Li P, Wang X, Romero CE, Pan L. Thermoeconomic analysis of a CO2 plume geothermal and supercritical CO2 Brayton combined cycle using solar energy as auxiliary heat source. J Clean Prod 2020;256:120374. https://doi.org/10.1016/j.jclepro.2020.120374.
[22] Manente G, Costa M. On the conceptual design of novel supercritical CO2 power cycles for waste heat recovery. Energies 2020;13:2219–31. https://doi.org/https://doi.org/10.3390/en13020370.
[23] Mohammadi K, McGowan JG. Thermoeconomic analysis of multi-stage recuperative Brayton cycles: Part II – waste energy recovery using CO 2 and organic Rankine power cycles. Energy Convers Manag 2019;185:920–34. https://doi.org/10.1016/j.enconman.2019.01.091.
[24] Manente G, Fortuna FM. Supercritical CO2 power cycles for waste heat recovery: a systematic comparison between traditional and novel layouts with dual expansion. Energy Convers Manag 2019;197:111777. https://doi.org/10.1016/j.enconman.2019.111777.
[25] Yang Z, Zhang H, Ni M, Lin B. A hybrid system using Brayton cycle to harvest the waste heat from a direct carbon solid oxide fuel cell. Appl Therm Eng 2019;160:113992. https://doi.org/10.1016/j.applthermaleng.2019.113992.
[26] Tracking IEA. Clean energy progress 2015. Paris: IEA; 2015. https://doi.org/https://www.iea.org/reports/tracking-clean-energy-progress-2015.
[27] Allam RJ, Fetvedt JE, Forrest BA, Freed DA. The OXY-fuel, supercritical CO2 allam cycle: new cycle developments to produce even lower-cost electricity from fossil fuels without atmospheric emissions. Proc. ASME Turbo Expo 2014. https://doi.org/10.1115/GT2014-26952.
[28] Crespi F, Gavagnin G, Sánchez D, Martínez GS. Supercritical carbon dioxide cycles for power generation: a review. Appl Energy 2017;195:152–83. https://doi.org/10.1016/j.apenergy.2017.02.048.
[29] Liu Y, Wang Y, Huang D. Supercritical CO2 Brayton cycle: a state-of-the-art review. Energy 2019;189:115900. https://doi.org/10.1016/j.energy.2019.115900.
[30] Guo J. Design analysis of supercritical carbon dioxide recuperator. Appl Energy 2016;164:21–7. https://doi.org/10.1016/j.apenergy.2015.11.049.
[31] Scaccabarozzi R, Gatti M, Martelli E. Thermodynamic analysis and numerical optimization of the NET Power oxy-combustion cycle. Appl Energy 2016;178:505–26. https://doi.org/10.1016/j.apenergy.2016.06.060.
[32] Purjam M, Goudarzi K, Keshtgar M. A new supercritical carbon dioxide Brayton cycle with high efficiency. Heat Transf Asian Res 2017;46:465–82.
[33] Padilla RV, Too YCS, Benito R, McNaughton R, Stein W. Thermodynamic feasibility of alternative supercritical CO2 Brayton cycles integrated with an ejector. Appl Energy 2016;169:49–62. https://doi.org/10.1016/j.apenergy.2016.02.029.
[34] Turchi CS, Ma Z, Neises TW, Wagner MJ. Thermodynamic study of advanced supercritical carbon dioxide power cycles for concentrating solar power systems. J Sol Energy Eng Trans ASME 2013. https://doi.org/10.1115/1.4024030.
[35] Liu Z, Liu Z, Cao X, Luo T, Yang X. Advanced exergoeconomic evaluation on supercritical carbon dioxide recompression Brayton cycle. J Clean Prod 2020;256:120537. https://doi.org/10.1016/j.jclepro.2020.120537.
[36] Alharbi S, Elsayed ML, Chow LC. Exergoeconomic analysis and optimization of an integrated system of supercritical CO2 Brayton cycle and multi-effect desalination. Energy 2020;197:117225. https://doi.org/10.1016/j.energy.2020.117225.
[37] Fan G, Li H, Du Y, Zheng S, Chen K, Dai Y. Preliminary conceptual design and thermo-economic analysis of a combined cooling, heating and power system based on supercritical carbon dioxide cycle. Energy 2020;203:117842. https://doi.org/10.1016/j.energy.2020.117842.
[38] Zhang F, Liao GEJ, Chen J, Leng E, Sundén B. Thermodynamic and exergoeconomic analysis of a novel CO2 based combined cooling, heating and power system. Energy Convers Manag 2020;222. https://doi.org/10.1016/j.enconman.2020.113251.
[39] Chen Y, Wang M, Liso V, Samsatli S, Samsatli NJ, Jing R, et al. Parametric analysis and optimization for exergoeconomic performance of a combined system based on solid oxide fuel cell-gas turbine and supercritical carbon dioxide Brayton cycle. Energy Convers Manag 2019;186:66–81. https://doi.org/10.1016/j.enconman.2019.02.036.
[40] Akbari AD, Mahmoudi SMS. Thermoeconomic analysis & optimization of the combined supercritical CO2 (carbon dioxide) recompression Brayton/organic Rankine cycle. Energy 2014;78:501–12. https://doi.org/10.1016/j.energy.2014.10.037.
[41] Wu C, Wang S, sen Li J. Exergoeconomic analysis and optimization of a combined supercritical carbon dioxide recompression Brayton/organic flash cycle for nuclear power plants. Energy Convers Manag 2018;171:936–52. https://doi.org/10.1016/j.enconman.2018.06.041.
[42] Ruiz-Casanova E, Rubio-Maya C, Pacheco-Ibarra JJ, Ambriz-Díaz VM, Romero CE, Wang X. Thermodynamic analysis and optimization of supercritical carbon dioxide Brayton cycles for use with low-grade geothermal heat sources. Energy Convers Manag 2020;216:112978. https://doi.org/10.1016/j.enconman.2020.112978.
[43] Kim S, Cho Y, Kim MS, Kim M. Characteristics and optimization of supercritical CO2 recompression power cycle and the influence of pinch point temperature difference of recuperators. Energy 2018;147:1216–26. https://doi.org/10.1016/j.energy.2017.12.161.
[44] Son S, Heo JY, Kim N Il, Jamal A, Lee JI. Reduction of CO2 emission for solar power backup by direct integration of oxy-combustion supercritical CO2 power cycle with concentrated solar power. Energy Convers Manag 2019;201:112161. https://doi.org/10.1016/j.enconman.2019.112161.
[45] Penkuhn M, Tsatsaronis G. Exergy analysis of the allam cycle. 5th Int Symp - Supercrit CO2 Power Cycles 2016;1–18.
[46] Rodríguez Hervás G, Petrakopoulou F. Exergoeconomic analysis of the allam cycle. Energy Fuel 2019;33:7561–8. https://doi.org/10.1021/acs.energyfuels.9b01348.
[47] Allam R, Martin S, Forrest B, Fetvedt J, Lu X, Freed D, et al. Demonstration of the allam cycle: an update on the development status of a high efficiency supercritical carbon dioxide power process employing full carbon capture. Energy Procedia 2017;114:5948–66. https://doi.org/10.1016/j.egypro.2017.03.1731.
[48] Onyebuchi VE, Kolios A, Hanak DP, Biliyok C, Manovic V. A systematic review of key challenges of CO2 transport via pipelines. Renew Sustain Energy Rev 2018;81:2563–83. https://doi.org/10.1016/j.rser.2017.06.064.
[49] Lu H, Ma X, Huang K, Fu L, Azimi M. Carbon dioxide transport via pipelines: a systematic review. J Clean Prod 2020;266:121994. https://doi.org/10.1016/j.jclepro.2020.121994.
[50] Cengel YA, Boles MA. Thermodynamics: an engineering approach. eighth ed. 2015. https://doi.org/10.1017/CBO9781107415324.004.
[51] Jing Q, Xie Y, Zhang D. Thermal hydraulic performance of printed circuit heat exchanger with various channel configurations and arc ribs for SCO2 Brayton cycle. Int J Heat Mass Tran 2020;150:119272. https://doi.org/10.1016/j.ijheatmasstransfer.2019.119272.
[52] Chai L, Tassou SA. Numerical study of the thermohydraulic performance of printed circuit heat exchangers for supercritical CO2 Brayton cycle applications. Energy Procedia 2019;161:480–8. https://doi.org/10.1016/j.egypro.2019.02.066.
[53] Hesselgreaves JE, Law R, Reay D. Compact heat exchangers, selection, design, and operation. 2 nd editi. Butterworth-Heinemann; 2016.
[54] Serrano IP, Cantizano A, Linares JI, Moratilla BY. Modeling and sizing of the heat exchangers of a new supercritical CO 2 Brayton power cycle for energy conversion for fusion reactors. Fusion Eng Des 2014;89. https://doi.org/10.1016/j.fusengdes.2014.04.039. 1905–8.
[55] Bejan A, Tsatsaronis G, Mortan M. Thermal design and optimization. Canada.

John Wiley & Sons; 1995.
[56] Jenkins S. Chemical engineering plant cost index annual average 2020. 2019.
[57] Weiland NT, Lance BW, Pidaparti SR. SCO2 power cycle component cost correlations from DOE data spanning multiple scales and applications. Proc ASME Turbo Expo 2019;9:1–18. https://doi.org/10.1115/GT2019-90493.
[58] Mathieu P, Nihart R. Zero-emission MATIANT cycle. J Eng Gas Turbines Power 1999;121:116–20. https://doi.org/10.1115/1.2816297.
[59] Yantovski EI, Zvagolsky KN, Gavrilenko VA. The COOPERATE-demo power cycle. Energy Convers Manag 1995;36:861–4. https://doi.org/10.1016/0196-8904(95)00139-5.
[60] McClung A, Brun K, Chordia L. Technical and economic evaluation of supercritical oxy-combustion for power generation. Pittsburgh, PA: Fourth Supercrit CO 2 Power Cycles Symp; Sept 2014.
[61] Zhang N, Lior N. A novel near-zero CO2 emission thermal cycle with LNG cryogenic exergy utilization. Energy 2006;31:1666–79. https://doi.org/10.1016/j.energy.2005.05.006.
[62] Gatewood J, Moore J, Ph D, Brun K, Ph D. The Texas cryogenic oxy-fuel cycle (TCO): a novel approach to power generation with CO2 options 2013: 1007–14. https://doi.org/https://doi.org/10.1115/GT2012-69930.
[63] Ricardo M. Co 2 capture in power plants-using the oxy-combustion principle. Norway: Norwegian University of Science and Technology; 2013.
[64] Sifat NS, Haseli Y. Thermodynamic modeling of Allam cycle. ASME Int Mech Eng Congr Expo Proc 2018;6A-144113:1–5. https://doi.org/10.1115/IMECE2018-88079.
[65] Hou S, Wu Y, Zhou Y, Yu L. Performance analysis of the combined supercritical CO2 recompression and regenerative cycle used in waste heat recovery of marine gas turbine. Energy Convers Manag 2017;151:73–85. https://doi.org/10.1016/j.enconman.2017.08.082.
[66] Mohammadi K, Ellingwood K, Powell K. A novel triple power cycle featuring a gas turbine cycle with supercritical carbon dioxide and organic Rankine cycles: thermoeconomic analysis and optimization. Energy Convers Manag 2020;220:113123. https://doi.org/10.1016/j.enconman.2020.113123.
[67] Doty S, Turner W. Energy management handbook. seventh ed. Lilburn, Georgia, USA: The Fairmont Press, Inc.; 2009.
[68] Wright S, Scammell W. Economics. Fundam. Appl. Supercrit. Carbon dioxide based power cycles. 2017. p. 127–45. https://doi.org/10.1016/B978-0-08-100804-1.00006-2.